

# Density Functional Calculations for III–V Diluted Ferromagnetic Semiconductors: A Review

Stefano Sanvito,<sup>1</sup> Gerhard Theurich,<sup>2</sup> and Nicola A. Hill<sup>1</sup>

*Received 1 November 2001*

---

In this paper we review the latest achievements of density functional theory in understanding the physics of diluted magnetic semiconductors. We focus on transition-metal-doped III–V semiconductors, which show spontaneous ferromagnetic order at relatively high temperature and good structural compatibility with existing III–V devices. We show that density functional theory is a very powerful tool for (i) studying the effects of local doping defects and disorder on the magnetic properties of these materials, (ii) predicting properties of new materials, and (iii) providing parameters, often not accessible from experiments, for use in model Hamiltonian calculations. Such studies are facilitated by recent advances in numerical implementations of density functional theory, which make the study of systems with a very large number of atoms possible.

---

**KEY WORDS:** diluted magnetic semiconductor; density functional theory.

## 1. INTRODUCTION

The possibility of using the spin degree of freedom as well as the electronic charge for electronic applications (“spintronics”) has received great attention in the last few years [1]. A prototypical application of this concept is the giant magnetoresistance (GMR) effect [2], where the electrical resistance of a magnetic multilayer is changed by the application of a magnetic field. GMR sensors are already commercially available for read heads in high density data storage devices, with performances increased by 1 order of magnitude with respect to conventional sensors. However current GMR sensors do not exploit completely the potential of spintronics. In existing electronic devices (for example, personal computers) there are two main elements: the logic components and the data storage device. The former are transistors based on semiconductor technology, while the latter is essentially a metallic magnetic film. Of course the ability to combine both logic elements and data storage in the same

device will open completely new possibilities, with huge potential applications. Hybrid structures, where magnetic metals are used to inject spin electrons into semiconductors have been shown to be problematic [3–5]. This is due to the large mismatch between the resistivities of semiconductors and metals, which seriously precludes effective spin injection [6]. Although this fundamental obstacle can be overcome, for instance by large contact resistances [7], it is natural to turn attention toward other directions and try to create all-semiconductor devices. These, of course, need magnetic semiconductors.

At present several types of diluted magnetic semiconductors (DMSs) are available [8]. Among these, the DMSs based on III–V semiconductors are particularly important because of their compatibility with existing III–V-based technology. III–V DMS are obtained by low-temperature molecular beam epitaxy (MBE) deposition of III–V semiconductors with a transition metal such as Mn. The nonequilibrium growth is necessary to prevent the formation of additional phases, and in general, only low concentrations of transition-metal ions can be incorporated in the nonmagnetic matrix. Nevertheless, despite the low concentrations, the systems develop long-range ferromagnetic order with remarkably high Curie

---

<sup>1</sup>Materials Department, University of California, Santa Barbara, California 93106.

<sup>2</sup>Department of Chemistry, University of Pennsylvania, Philadelphia, Pennsylvania 19104.

temperatures  $T_c$ . For the known III–V-based DMS the highest Curie temperatures obtained are  $T_c \sim 30$  K for (In,Mn)As [8,9],  $T_c = 110$  K for (Ga,Mn)As [8], and, very recently, a report of  $T_c = 940$  K for (Ga,Mn)N [10]. Moreover, although this paper is focused only on the III–V DMS, it is worth mentioning that ferromagnetism with  $T_c$  often above room temperature has been found in several other DMSs, including  $\text{Ge}_{1-x}\text{Mn}_x$  [11],  $\text{Cd}_{1-x}\text{Mn}_x\text{GeP}_2$  [12],  $\text{Ti}_{1-x}\text{Co}_x\text{O}_2$  [13], and  $\text{Zn}_{1-x}\text{Co}_x\text{O}$  [14].

(Ga,Mn)As, although it has a  $T_c$  far below room temperature, is the most widely studied DMS. This is due to its structural compatibility with most epitaxially grown III–V's, which makes it ideal for building heterostructures and exploring new device concepts. Examples that have been already achieved include spin injection into heterostructures [15] and field-effect control of the ferromagnetism [16].

Three important features underlie the ferromagnetic order of (Ga,Mn)As, and these are shared by the other Mn-doped III–V DMSs: (i)  $\text{Mn}^{2+}$  ions substitute for  $\text{Ga}^{3+}$  cations in the zinc blende lattice, providing localized spins ( $S = 5/2$  in  $\text{Ga}_{1-x}\text{Mn}_x\text{As}$  and  $\text{In}_{1-x}\text{Mn}_x\text{As}$ ), (ii) there are free holes in the system although the actual concentration is much smaller than the Mn concentration (despite the nominal valence suggests that the two concentrations should be identical), and (iii) the hole spins couple antiferromagnetically with the Mn spins, owing to a dynamic p–d coupling. Then the ferromagnetic behavior can be reasonably well described by the Zener model [17], in which antiferromagnetic exchange coupling partially spin polarizes the holes, which in turn cause an alignment of the local Mn spins. Within the Zener model, the interaction Hamiltonian between the hole spin  $\vec{s}$  and the Mn spin  $\vec{S}$  is

$$H = -N_0\beta\vec{s} \cdot \vec{S}, \quad (1)$$

where  $N_0$  is the concentration of the cation sites and  $\beta$  is the p–d exchange integral.  $N_0\beta$  is usually called the exchange constant. If one simply uses the mean field approximation [17,18], in which the magnetizations of both carriers and Mn ions are considered to be uniform in space, we obtain an expression for  $T_c$ :

$$T_c = \frac{xN_0S(S+1)\beta^2\chi_s}{3k_B(g^*\mu_B)^2}, \quad (2)$$

where  $\chi_s$  is the magnetic susceptibility of the free carriers (holes in this case),  $g^*$  is their  $g$ -factor,  $k_B$  is the Boltzmann constant, and  $\mu_B$  is the Bohr magneton.

The result of Eq. (2) can be greatly refined by including a detailed description of the band structure of the underlying nonmagnetic semiconductors or by incorporating correlation effects going beyond the mean field approximation. However, it is important to stress that the use of these models *always* requires parameters that are often difficult to extract from the experiments. For example the experimental value of the exchange constant  $N_0\beta$  vary in the range 1–3 eV [19–24].

In addition, models based on any kind of mean field approximation naturally fail in describing local effects, which occur on the atomic scale. The ferromagnetism of (Ga,Mn)As is very sensitive to the sample “history,” such as the growth conditions [8] and eventual after-growth processing [25,26]. Since the growth dynamics certainly affects the microscopic configuration of the samples, this suggests that knowledge of the local chemical environment is crucial for understanding and modeling the properties correctly.

These considerations show that it is essential to have a microscopic theory providing information to the simpler mean field-like models. Density functional theory (DFT) [27,28] is to date the most efficient and accurate microscopic theory for describing the electronic, magnetic, and structural properties of the ground state of electronic systems with a large number of degrees of freedom. Recent advances in the numerical implementations, mainly concentrated in the use of improved pseudopotentials [29], of efficient basis sets [30] and of  $N$  order approximations [31], make possible the study of systems containing several hundreds of atoms. Such computational capabilities are required to study the DMSs in the low concentration limit. The main aim of this paper is to provide a review of the achievements of DFT in describing the properties of the DMSs. In particular we will show that DFT is an invaluable tool for (i) studying the effects of local doping defects and disorder on the magnetic properties, (ii) predicting properties of new materials, and (iii) providing parameters, often not accessible from experiments, for use in model Hamiltonian calculations.

The remainder of the paper is organized as follows. First, we will briefly overview the most recent developments in density functional theory. In the following section we will discuss the structural properties of (Ga,Mn)As and explain why zinc blende MnAs cannot be grown. Moreover we will also look at spin–orbit effects and explain why this introduces only minor quantitative changes in the exchange constant of (Ga,Mn)As. Then we will move to the low

dilution limit, calculating the exchange constants and discussing the limitations of mean field models. In the remaining sections we will consider the effects of the local microscopic configuration of the Mn ions and possible intrinsic defects on the ferromagnetism of (Ga,Mn)As. In particular we will look at the role of intrinsic defects and at the transport properties of digital ferromagnetic heterostructures (DFH) [32]. Finally we will overview theoretical predictions for new materials and then we will conclude.

## 2. DENSITY FUNCTIONAL THEORY

Since its introduction in the 1960s [27,28] density functional theory has evolved into a powerful tool that is widely used in condensed matter theory and computational materials for the calculation of electronic, magnetic, and structural properties of solids. The method has been remarkably successful in predicting, reproducing, and/or explaining a wide variety of materials phenomena. Specific examples range from early predictions of phase transitions in silicon as a function of pressure [33] to determination of stable and metastable adsorption geometries on metal surfaces [34] as well as many successes in understanding the behavior of magnetic materials, including those described in this work.

The density functional formalism is based on the theorem that for an interacting inhomogeneous electron gas in a static external potential  $v(\mathbf{r})$ , there exists a universal functional of the density,  $F[\rho(\mathbf{r})]$ , independent of  $v(\mathbf{r})$ , such that the expression

$$E = \int v(\mathbf{r})\rho(\mathbf{r}) d\mathbf{r} + F[\rho(\mathbf{r})] \quad (3)$$

has as its minimum value, the correct ground state energy associated with  $v(\mathbf{r})$  [27].

The true density  $\rho(\mathbf{r})$  can in principle be exactly obtained from the solution of an associated single-particle problem, whose effective single-particle potential  $v_{\text{eff}}[\rho(\mathbf{r})]$  is a unique functional of  $\rho(\mathbf{r})$  [28]. As a consequence, the many-electron ground state reduces to that of a one-electron Schrödinger equation:

$$\left[ -\frac{1}{2}\nabla^2 + v(\mathbf{r}) + \int \frac{\rho(\mathbf{r}')}{|\mathbf{r}-\mathbf{r}'|} d\mathbf{r}' + \frac{\delta E_{\text{xc}}}{\delta \rho(\mathbf{r})} \right] \phi_i(\mathbf{r}) = \varepsilon_i \phi_i(\mathbf{r}), \quad (4)$$

where

$$\rho(\mathbf{r}) = \sum |\phi_i|^2. \quad (5)$$

The so-called Kohn–Sham wave functions  $\phi_i$  are single-particle eigenfunctions that are strictly meaningful only for determining  $\rho(\mathbf{r})$ , and the Kohn–Sham eigenvalues  $\varepsilon_i$  are the derivatives of the total energy with respect to the occupation of state  $i$ . Note that they are not strictly related to single-particle excitation energies, although the Kohn–Sham band structure can sometimes be a useful tool in the interpretation of photoemission (or similar) data.

For an arbitrary density there is no simple exact expression for the exchange-correlation energy  $E_{\text{xc}}$ , and so to make progress, the so-called local density approximation (LDA) is often made. Within the LDA,  $E_{\text{xc}}$  is written as

$$E_{\text{xc}}[\rho] = \int \rho(\mathbf{r})\epsilon_{\text{xc}}(\rho(\mathbf{r})) d\mathbf{r} \quad (6)$$

where  $\epsilon_{\text{xc}}$  is the exchange-correlation energy per electron of a uniform interacting electron gas of the same density  $\rho$ . The LDA is strictly valid only if  $\rho(\mathbf{r})$  is slowly varying, and many extensions exist which give improved accuracy for systems with localized electrons.

Density functional calculations for magnetic materials became widespread in the late 1970s, with a number of studies of third and fourth row transition metals [35–37]. These studies established that the local density approximation gives results that are in reasonable agreement with experiment for quantities such as cohesive energy, bulk modulus, and magnetic moments, provided that spin polarization is included explicitly by extending the LDA to the local spin density approximation (LSDA). They also noted, however, that the calculated properties are very sensitive to details of the structure and magnetic ordering, which can lead to discrepancies between the LSDA results and experiment. The most notorious of these is the well-known prediction of the incorrect ground state of iron (face-centered cubic and antiferromagnetic, rather than the correct body-centered cubic and ferromagnetic) by the LSDA.

A number of technical developments have facilitated the study of magnetic materials, perhaps the most important being the introduction of the fixed spin moment (FSM) method [38,39]. In the FSM method the ground state of a constrained system with a fixed magnetic moment is calculated. Not only does this speed up the convergence, but the total energy *surface* in magnetic moment/volume space can be determined, giving additional information particularly about metastable magnetic phases. Also, implementation of Gaussian smearing [40] and related

schemes have helped to speed up the convergence of calculations for magnetic metals with partially filled d bands and complex Fermi surfaces, in which it is difficult to carry out integrals over the occupied part of the Brillouin Zone.

In parallel with these technical developments, extensions and improvements to the LSDA have also been explored. The usual generalized gradient (GGA) and weighted density (WDA) approximations that give improved results for nonmagnetic systems do not tend to give systematic improvement for magnetic materials, although the GGA does at least predict the correct ground state for iron. For more information about these approximations, see Ref. [41] and references therein. Methods such as the LDA+U [42,43], and self-interaction correction [44] are specifically tailored to treat strongly correlated systems, and therefore are more appropriate for magnetic systems with narrow d or f bands.

## 2.1. Codes Available

There are many excellent computer programs available today for performing density functional theory calculations. These use a range of different methodologies, have different specialties, and are widely varying in cost (both in dollar amount and in their computer requirements). In this section we describe some of the most popular programs.

Many DFT programs are based on the so-called plane-wave pseudopotential (PWPP) method [33], in which the wave functions are expanded in a plane-wave basis, and the electron-ion interaction is modeled by a pseudopotential. Plane-wave basis sets offer many advantages in DFT calculations for solids, including completeness, an unbiased representation, and arbitrarily good convergence accuracy. Publically available PWPP codes include DoD Plane wave [45], which is a general-purpose scalable plane-wave basis density functional code that treats insulators, semiconductors, metals, and magnetic materials; ABINIT [46], which allows both DFT and density functional perturbation theory calculations; and SPINOR [47], which extends the usual LSDA formalism to include spin-orbit coupling and generalized noncollinear magnetism. Both ABINIT and SPINOR are PWPP codes and are available under the GNU General Public License [48]. One of the most popular “semicommercial” PWPP codes is the VASP package [49] developed at the University of Vienna, Austria. VASP allows DFT and molecular dynamics

calculations, and is quite fast because of its use of ultrasoft pseudopotentials. The developers charge a nominal fee for the source code, and require authorship on the first publication using the code. There are also a number of fully commercialized density functional codes that are targeted in large part at chemical and pharmaceutical companies. For example, Accelerlys [50] markets the PWPP CASTEP code [51].

For systems involving a large number of atoms in the unit cell, plane-wave-based DFT algorithms are not ideal because of the large computational overheads involved. For this purpose it is convenient to use codes based on localized atomic orbital basis sets, although their numerical implementation is usually quite complicated. Most of the results of this paper are obtained with the code SIESTA [52,53], which combines pseudopotential techniques with a pseudoatomic orbital basis set [30]. The code is highly optimized to deal with large systems, and both efficient order  $N$  methods and molecular dynamics tools are available. The developers require an initial collaboration and coauthorship on works produced by SIESTA.

Traditionally, however, magnetic materials have been studied using all-electron methods with mixed basis sets, such as the linear augmented plane wave (LAPW) [41], linear muffin tin orbital (LMTO) [54], or Korringa-Kohn-Rostoker (KKR) [55] approaches. Again many codes are available. For example, the Vienna University of Technology produces a full-potential LAPW code called WIEN97 [56] which is a highly accurate, all-electron code that includes relativistic effects. A small (\$350 at press time) fee is charged. The Stuttgart LMTO program [57] is a fast and efficient tool for calculation of charge- and spin-self-consistent band structures, partial densities of states, Fermi surfaces, total energies, and the partial pressures. In addition, the program delivers tools for analyzing the electronic structure and chemical bonding such as orbital-projected band structures, crystal orbital Hamiltonian populations, and electron localization functions.

## 3. ZINC BLENDE MnAs

As we mentioned in the Introduction, so far Mn has been incorporated in GaAs only at concentrations smaller than 7%. Considering that the Zener model predicts that  $T_c$  increases with  $x$  (see Eq. (2)), this poses a severe limit to the highest Curie temperature obtainable. It is therefore of great interest to investigate if there are some conditions, which

allow the growth of (Ga,Mn)As with higher Mn concentration or even ultimately zinc blende MnAs. In this section we describe DFT calculations from the literature that investigate both the stability and the electronic and magnetic properties of the zinc blende MnAs.

Several groups have calculated the electronic structure of zinc blende MnAs by using both the LSDA [58–61] and the GGA [62] approximations for the exchange-correlation potential. The calculated lattice constant  $a_0$  for zinc blende MnAs is found to be around 5.6–5.7 Å. This result, also confirmed by relaxation calculation of (Ga,Mn)As [63], is quite appealing since a hypothetical zinc blende MnAs appears to have a lattice constant very close to that of GaAs ( $a_0 = 5.6533$  Å). These results seem to conflict with the extrapolation to  $x = 1$  (assuming Vegard’s law) of the lattice constant of  $\text{Ga}_{1-x}\text{Mn}_x\text{As}$  and  $\text{In}_{1-x}\text{Mn}_x\text{As}$  [8], which give respectively  $a_0 = 5.98$  Å and  $a_0 = 6.01$  Å. However, it is worth noting that the lattice constant has been measured only for  $x \ll 1$  and that a linear extrapolation to  $x = 1$  may not be valid. Moreover in real (Ga,Mn)As samples the presence of intrinsic defects (mainly As antisites  $\text{As}_{\text{Ga}}$ ) can play an important role in determining the structural properties. This is clearly demonstrated in low-temperature annealing experiments [25,26], where the lattice constants of samples with the same Mn concentration change, depending on annealing conditions (temperature and time).

It is also important to point out that generally the LDA approximation underestimates the equilibrium lattice constant, in particular if strong p–d hybridization is present. This is probably the situation for zinc blende MnAs, although the good agreement with experiments for a different MnAs lattice structure (the NiAs-type structure) gives confidence in the LSDA results. Furthermore a recent LDA+U calculation [64] (LDA+U usually corrects the tendency to overbinding of the LDA) finds a lattice constant for MnAs very similar to that of GaAs [65]. This suggests that LDA provides a good description of, at least, the structural properties. Finally we must point out that a much larger lattice constant ( $a_0 = 5.9$  Å) has been found by Shirai *et al.* [58,61] within the LSDA. However this is probably due to an artifact of the minimization procedure used.

Turning our attention to the electronic properties, in Fig. 1 we present our calculated band structure for MnAs at the LDA equilibrium lattice constant  $a_0 = 5.7$  Å from Ref. [60]. The results are obtained with the code SPINOR [47]. Calculations by other

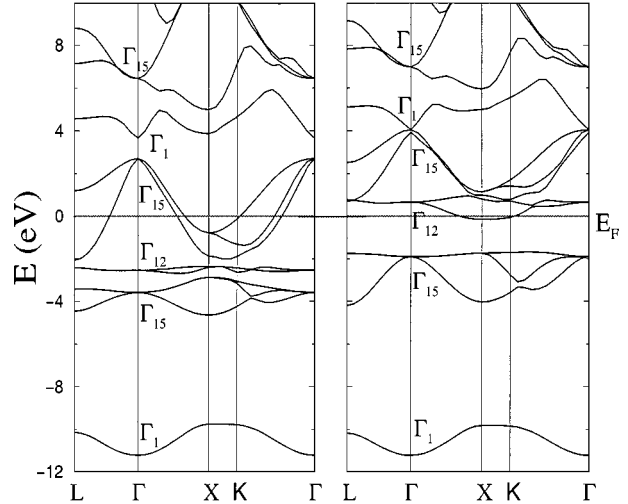


**Fig. 1.** Band structure for zinc blende MnAs at the LDA energy minimum ( $a_0 = 5.7$  Å). The figure on the left corresponds to the majority spin and the one on the right to the minority spin. The horizontal line denotes the position of the Fermi energy, which has been chosen to be 0 eV.

groups at similar lattice constants give similar band structures [62]. We first note that, excluding the presence of the Mn d bands, the band structure closely resembles that of the nonmagnetic III–V semiconductors. If we consider the majority band first, we can easily identify the As p valence band (first  $\Gamma_{15}$  point above  $E_F$ ) and the first of the conduction bands (first  $\Gamma_1$  point above  $E_F$ ). However the strong interaction with the Mn d states pushes the former toward higher energies and they become half-filled. The Mn d bands which are split into the doubly degenerate e band ( $\Gamma_{12}$ ) and the triply degenerate  $t_2$  band ( $\Gamma_{15}$ ) are below the Fermi energy and entirely occupied. In contrast, in the minority band there is a large split between the  $t_2$  and the e states, which gives rise to a large gap in the band structure.

It is very important to note that at this lattice constant the Fermi energy in the minority spin band cuts through the edge of the Mn d (e) states. This suggests that a tiny expansion of the structure, reducing the Mn d (e) bandwidth, will move the Fermi energy into the minority spin gap. In fact we have predicted [60] that for a lattice constant larger than  $a_0 = 5.8$  Å zinc blende MnAs will be a half-metal. This result, confirmed by other calculations [58,59,61], is very attractive since half-metallic systems are sources of fully spin-polarized currents. We therefore investigate if there are conditions under which such a zinc blende phase of MnAs can be grown.

### 3.1. MnAs: Zinc Blende vs. NiAs-Type Structure

The main obstacle to the growth of zinc blende MnAs is its instability with respect to the NiAs structure. The NiAs-type structure is a hexagonal structure (space group  $P6_3/mmc$ ) with six-coordinated Mn. We have studied the relative stability of the NiAs-type and the zinc blende structures by comparing the total energy per MnAs pair as function of the unit cell volume [60]. The results are presented in Fig. 2. It is clear that the NiAs-type structure has a much lower total energy and also a denser lattice. Therefore it is the stable structure at all thermodynamically accessible pressures. However we note that if the lattice is forced to expand there is a crossover between the two structures, with the zinc blende being favorable for volumes larger than  $\sim 47 \text{ \AA}^3$  per MnAs pair. This corresponds to a lattice constant for the zinc blende structure of  $a_0 = 5.8 \text{ \AA}$ , the same at which the transition to half-metal occurs. Therefore there is the hope that zinc blende MnAs could be grown if “negative pressure” were applied, for example if it were grown on a substrate with large lattice mismatch. Unfortunately this is also very challenging.

In the inset of Fig. 2 we show the total energy as a function of the ratio between the two lattice constants of the NiAs-type structure ( $c/a$  ratio) at constant volume (the experimental volume). The figure shows that the NiAs-type structure can accommodate large

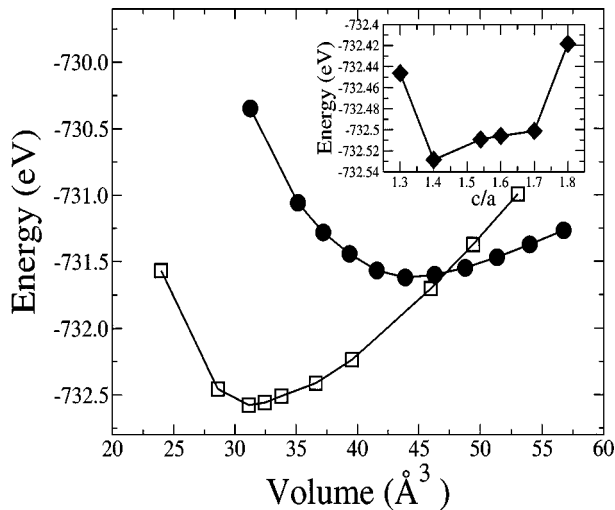


**Fig. 2.** Total energy as a function of the MnAs pair volume for the NiAs-type (squares) and the zinc blende (circles) structure. Note the large stability of the NiAs-type structure over a very broad volume range. In the inset we present the same quantity for the NiAs-type structure as a function of  $c/a$ .

structural distortions without corresponding large energy costs (the total energy changes of only about 20 meV when going from  $c/a = 1.7$  to  $c/a = 1.4$ ). This means that at equilibrium it is energetically more favorable for the system to distort the cell, instead of increasing the volume and inducing a NiAs-type to zinc blende transition. In conclusion DFT calculations have shown that zinc blende MnAs would indeed have desirable properties but that it is unstable and will always tends to form the less attractive NiAs phase. Results analogous to those presented here are obtained for MnBi [60], MnSb, and MnP [62], suggesting that the low solubility limit of Mn is a characteristic of all the III-V’s.

### 3.2. The Effect of Spin–Orbit Coupling

The commonly used p–d interaction Hamiltonian for dilute magnetic semiconductors is of the Kondo form given in Eq. 1. The strength of the interaction is governed by the exchange constant  $N_0\beta$ . In this section we will address the question of how  $N_0\beta$  is affected by the spin–orbit coupling.

Despite the formal similarity of Eq. (1) to a Heisenberg exchange interaction the p–d interaction in DMS materials does not originate from the Coulomb interaction but arises as a result of the hybridization between p and d derived bands in the crystal. The appropriate Hamiltonian to describe transition-metal impurities in a host crystal is the well-known Anderson Hamiltonian. However, Schrieffer and Wolff have shown that the Anderson Hamiltonian can be transformed into a Kondo-like form [66], containing a term similar to that of Eq. (1). This transformation relates the effective exchange integral ( $\beta$ ), which will be negative in general, to the matrix elements of the interaction potential between the bands of the crystal. We will discuss the results of this section using the following model Hamiltonian for the valence band states:

$$H = H_0 + H_X^{\text{pd}} + H_{\text{soc}}. \quad (7)$$

Here  $H_0$  is the crystal Hamiltonian without p–d and without spin–orbit interaction.  $H_X^{\text{pd}}$  is the p–d interaction given by Eq. (1) and  $H_{\text{soc}}$  is the spin–orbit interaction.

Naturally, if the potential changes, the hybridization between the bands will be affected and thus the effective exchange integral will change accordingly. Note that if  $\beta$  were a “real” Coulomb exchange integral it would not be directly affected by a change

in the potential. Only a very small indirect effect due to the change of the self-consistent charge distribution would be expected in that case.

In the (Ga,Mn)As crystal the As anions introduce a substantial spin–orbit interaction which is about 1 order of magnitude smaller than the exchange constants determined within scalar-relativistic calculations. In state-of-the-art scalar-relativistic density functional calculations, spin–orbit coupling is taken into account only effectively by using averaged potentials, which conserve all nonrelativistic symmetry properties of the electronic states in the crystal. However in practice the symmetry relations change drastically when spin–orbit coupling is considered for a spin-polarized system.

There are two questions to be answered. First, is it still possible to transform a hybridization interaction into the Kondo form when the potential becomes spin dependent, as is the case when spin–orbit coupling is included explicitly? Second, if the Kondo form still holds, how much will the exchange constant change due to the change in the potential? In order to answer these questions we performed density functional calculations based on fully relativistic pseudopotentials [67] for GaAs and MnAs, using the code SPINOR. Naturally the obtained density functional results are fully self-consistent and do not lend themselves easily to discuss individual terms of the model Hamiltonian introduced in Eq. (7) separately. We therefore proceed in the opposite direction and check whether the density functional results can be interpreted by the model Hamiltonian.

We assume that  $H_0$  of Eq. (7) has been solved for the valence band states at the Brillouin zone center. For scalar-relativistic band structures of zinc blende semiconductors such as GaAs, the valence band top is six times degenerate. This is also the case for the magnetic system MnAs as long as  $H_X^{\text{pd}}$  is turned off. However, when  $H_X^{\text{pd}}$  is turned on, the p-like states at the top of the valence band will split according to their spin orientation into two groups of triply degenerate states, separated by the energy  $N_0\beta\langle S_z \rangle$ , following Eq. (1) (see also the discussion of Section 4.2). Here  $\langle S_z \rangle$  is the z-component of the spin polarization per unit cell. This is the result found by the scalar-relativistic approach. Finally, treating  $H_{\text{soc}}$  as a perturbation, all remaining degeneracies are lifted by first-order energy corrections, as is shown in Fig. 3. Note that the second-order corrections are only of order 1 meV for typical values of  $\Delta$ , the spin–orbit splitting of the valence band at  $\Gamma$ , and  $B = \frac{1}{6}N_0\beta\langle S_z \rangle$ .

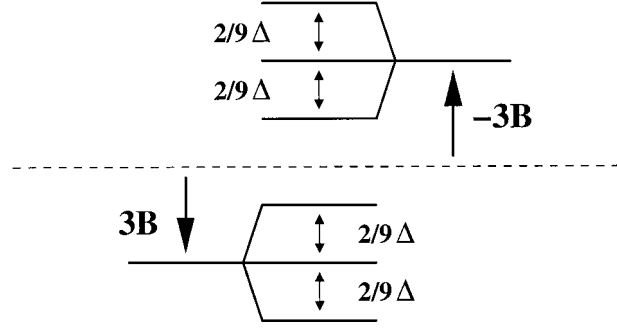


**Fig. 3.** Exchange and spin–orbit splitting of the valence band top in MnAs. The split of the center of the band is  $6B$ , where  $B = \frac{1}{6}N_0\beta\langle S_z \rangle$ .

Now let us turn to the density functional results. Table I lists the the scalar and fully relativistic valence band edge energies for MnAs. The DFT calculations confirm the model discussed above in that all scalar-relativistic degeneracies are lifted when spin–orbit coupling is included explicitly. We also find that, in both groups, one state lies approximately at the same energy as the scalar-relativistic degeneracy, as predicted by the model. However, the energy difference between the three minority states is approximately 50 meV, whereas the same number for the majority states is found to be approximately 100 meV. According to Fig. 3 the model predicts a splitting of  $\frac{2}{9}\Delta$  for minority and majority states alike, which is approximately 80 meV, using the GaAs spin–orbit splitting for  $\Delta$ . Hence the model and density functional results show significant discrepancies of about 30%, which would indicate that the model Hamiltonian of Eq. (7), and therefore the Kondo form of the p–d interaction, is questionable for MnAs when spin–orbit coupling is taken into account explicitly. However, the deviations are about 2 orders of magnitude smaller than the splitting between the majority and minority states. Hence the corrections due to spin–orbit coupling affect the exchange constant  $N_0\beta$  for MnAs only in the order of 1%.

**Table I.** Top of the Valence Band Levels for MnAs at the Brillouin Zone Center Determined by Density Functional Method with and Without Spin–Orbit Coupling

	Minority (eV)	Majority (eV)
Without $H_{\text{soc}}$	-2.405	2.405
With $H_{\text{soc}}$	-2.355	2.499
With $H_{\text{soc}}$	-2.408	2.399
With $H_{\text{soc}}$	-2.458	2.308

The model Hamiltonian given in Eq. (7) thus remains a good approximation for the high concentration limit as was shown for MnAs. However, there are two important issues when the Mn concentration is lowered. First, as the splitting between the minority and majority valence band top becomes smaller the observed deviations between the model and the density functional results will become increasingly important. There might be a point reached where the Kondo form of the p-d interaction given in Eq. (1) breaks down. This argument, however, is based on a mean field extrapolation into the low density regime. Results presented in Section 4 of this paper indicate that a mean field approximation might be invalid for the p-d interaction in dilute magnetic semiconductors altogether.

Second, as the Mn concentration decreases, the band structure, especially around the top of the valence band, becomes strongly dominated by spin-orbit effects. Hence, scalar-relativistic results in the low density limit need to be interpreted very carefully, especially when spin dynamics is considered.

#### 4. Ga<sub>1-x</sub>Mn<sub>x</sub>As IN THE DILUTED LIMIT

The first principal study of Ga<sub>1-x</sub>Mn<sub>x</sub> in the low dilution limit is a formidable theoretical challenge. This is due to the large number of atoms that one should include in the unit cell in order to reproduce the experimental Mn concentrations. However several numerical implementations of DFT capable of dealing with a large number of atoms are now available. These are generally based on the use of pseudopotentials [29] and on localized basis sets [30]. Most of the results we will present in the following sections are obtained with the code SIESTA [31,52,53], which combines both of these features.

##### 4.1. Electronic and Magnetic Properties

We start by analyzing the calculated density of states (DOS) of a 64-atom GaAs unit cell containing one Mn<sub>Ga</sub> substitution (Fig. 4) [68]. This corresponds to  $x = 0.03125$ , an experimentally accessible concentration. From the figure it is clear that Ga<sub>1-x</sub>Mn<sub>x</sub>As has the electronic structure of a half-metal. This result is largely confirmed by all density functional calculations to date both using the LDA [63,69,70] and the GGA [71] approximation. It is also the same structure found for In<sub>1-x</sub>Mn<sub>x</sub>As [72]. If we project the density

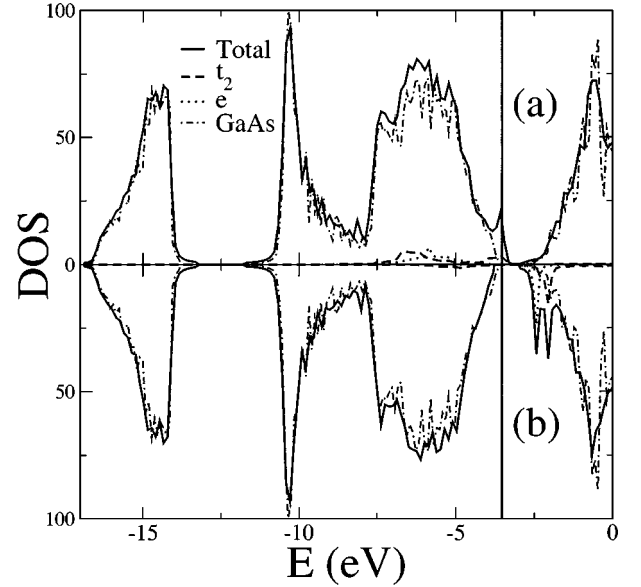


**Fig. 4.** Partial density of states for Ga<sub>1-x</sub>Mn<sub>x</sub>As for  $x = 0.03125$  (one Mn<sub>Ga</sub> in a 64-atom GaAs cell): (a) majority spin and (b) minority spin. The vertical line denotes the position of the Fermi energy.

of states onto the different orbital components (partial density of states, PDOS) some additional features are revealed. The majority band exhibits two broad peaks between  $-4$  and  $-1$  eV below the Fermi energy, with strong Mn d (e) and  $t_2$  components respectively. In addition there is a rather narrow  $t_2$  peak at the Fermi energy. In contrast, the minority band has almost no d character below  $E_F$  but instead has two sharp e and  $t_2$  peaks around 1 eV above  $E_F$ . The different peak widths reflect the different degrees of hybridization of the Mn d subbands with the GaAs bands.

The magnetic moment of the unit cell is  $4\mu_B$ , and remains the same up to concentrations of the order of  $x = 0.5$  [71]. An integer number for the magnetic moment is consistent with the half-metallicity seen in the DOS. At this point it is therefore very relevant to discuss the atomic configuration of Mn in GaAs. The band structure around the  $\Gamma$  point for  $x = 0.03125$  Ga<sub>1-x</sub>Mn<sub>x</sub>As (1 Mn ion in a cubic 64 atom GaAs cell) is presented in Fig. 5, along with the orbital resolved DOS at the  $\Gamma$  point. We consider the band structure only along the direction  $(\frac{1}{8}\frac{\pi}{c_0}, 0, 0) \rightarrow (0, 0, 0) \rightarrow (\frac{1}{8}\frac{\pi}{c_0}, \frac{1}{8}\frac{\pi}{c_0}, \frac{1}{8}\frac{\pi}{c_0})$ , with  $c_0$  being the unit vector of the cubic cell. We indicate these two directions respectively as  $X$  and  $M$ .

From the picture it is very clear that the Fermi energy cuts through the top of the valence band for the majority spin. This, in addition to the fact that all the

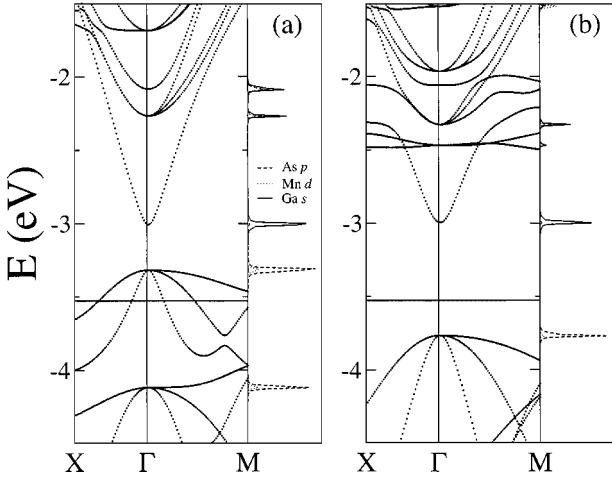


**Fig. 5.** Band structure and orbital resolved DOS at the  $\Gamma$  point for  $\text{Ga}_{1-x}\text{Mn}_x\text{As}$  with  $x = 0.03125$  (1 Mn ion in a cubic 64-atom GaAs cell): (a) majority band and (b) minority band. The horizontal line denotes the position of the Fermi energy.

Mn d states in the majority spin band are occupied, suggests that Mn in GaAs is incorporated as  $\text{Mn}^{2+}$  and that there is a polarized hole, which is antiferromagnetically coupled to the Mn. The presence of a hole is revealed by an accurate analysis of the integrated DOS [69], and a signature of the antiferromagnetic coupling is the fact that the induced magnetic moment at the As sites is antiparallel to that of the Mn ions [68,71].

It is important to stress that the results from DFT are not as ideal as the atomic-like picture discussed above, which predicts  $S = 5/2$  for the Mn. Mulliken population analysis [68,73,74] shows that the population of the Mn d orbital is 4.7 and 0.7 electronic charges respectively for the majority and minority states. Considering the fact that the overlap population is of the order of 0.7, the raw data are compatible with both Mn  $d^4$  and  $d^5$ . Moreover we must stress that at the top of the valence band there is a quite large hybridization between Mn d and As p states. All these factors contribute to reduce the magnetic moment from  $5\mu_B$  ( $S = 5/2$ ) expected from the atomic-like picture to  $4\mu_B$ . A magnetic moment of  $4\mu_B$  appears to be smaller than that found experimentally ( $\sim 4.4\mu_B$ ) [75], although the agreement can be restored by considering partial hole compensation as we will show in the following sessions.

The behavior of Mn in GaAs seems to be similar to that of Mn substituting the cation sites in other III–V semiconductors, and in II–VI and group IV semiconductors. Schulthess and Butler [69] have

calculated the electronic structure of Mn in GaAs, Ge, ZnSe, and ZnO. The main results are that (i) the number of minority electrons is not changed by the Mn impurity and (ii) each Mn impurity adds five additional majority states to the valence band. This leads to a magnetic moment of  $3\mu_B$ ,  $4\mu_B$ , and  $5\mu_B$  respectively for Mn in Ge, GaAs, and both ZnSe and ZnO.

It is difficult to extract the localization properties of the holes introduced by the Mn ions from DFT calculations. In particular we are not able to conclusively establish whether or not the holes are bound to  $\text{Mn}^{2+}$  forming a neutral ( $3d^5 + h$ ) complex [19]. On the one hand plots of the charge density obtained from states within 0.5 eV around the Fermi energy reveal that most of the charge is concentrated around the Mn sites [68]. This seems to suggest localization of the hole around the Mn ion. On the other hand accurate valence band fitting [63] reveals an effective mass quite similar to that of GaAs. This is of course an indication of delocalization. We believe that this point needs further investigation. A key element to determining the localization properties of the holes is a knowledge of the exchange constant  $N_0\beta$ , which we discuss in the next section.

## 4.2. The Exchange Coupling

We calculate the exchange constant by evaluating the spin splitting of the conduction and valence bands. This mimics a typical magneto-optical experiment [21]. The main idea is that in the mean field theory based on the Hamiltonian of Eq. (1) the spin splitting of the valence band depends linearly on both the exchange constant  $N_0\beta$  and the Mn concentration  $x$  [68]. The same argument holds for the spin splitting of the conduction band, which is regulated by a similar Hamiltonian with exchange constant  $N_0\alpha$ . Therefore the exchange constants can be directly computed from the conduction band-edge (valence band-edge) spin-splittings  $\Delta E^c = E_\downarrow^c - E_\uparrow^c$  ( $\Delta E^v = E_\downarrow^v - E_\uparrow^v$ ) as follows:

$$N_0\alpha = \Delta E^c/x\langle S \rangle, \quad N_0\beta = \Delta E^v/x\langle S \rangle, \quad (8)$$

where  $\langle S \rangle$  is half of the computed magnetization per Mn ion.

Recalling the fact that (Ga,Mn)As has a direct gap at the  $\Gamma$  point, we calculate the band structure of  $\text{Ga}_{1-x}\text{Mn}_x\text{As}$  supercells (see Fig. 5) around the  $\Gamma$  point for different Mn concentrations, and extract the exchange constants by using Eqs. (8). Our results are in Table II.

**Table II.** Conduction  $\Delta E^c$  and Valence  $\Delta E^v$  Band-Edge Spin Splitting, and Exchange Constants as a Function of the Mn Concentration  $x$  for  $\text{Ga}_{1-x}\text{Mn}_x\text{As}$

$x$	$\Delta E^c$ (eV)	$\Delta E^v$ (eV)	$N_0\alpha$ (eV)	$N_0\beta$ (eV)
0.06250	0.0339	-0.6839	0.272	-5.48
0.04166	0.0248	-0.5458	0.298	-6.54
0.03125	0.0105	-0.4472	0.168	-7.34
0.02084	0.0099	-0.3442	0.234	-8.16

The behaviors of the valence and conduction bands are remarkably different. For the conduction band, although the spin splitting shows large fluctuations with  $x$ , there is no systematic variation with the Mn concentration. This indicates that the mean field approximation that led to Eq. (8) is appropriate and one can conclude that the exchange coupling between electrons in the conduction band and the Mn is ferromagnetic with an exchange constant  $N_0\alpha \sim 0.2$  eV. This is expected since the coupling in this case is direct (Coulombic s-d coupling). Note also that the value of the exchange constant  $N\alpha$  is very close to that usually found in II-VI semiconductors [76].

In contrast the valence band shows strong deviation from the mean field expression (8), since the valence band spin splitting does not vary linearly with  $x$ . Turning the argument around,  $N_0\beta$  increases with decreasing Mn concentration, a behavior already well known to occur in  $\text{Cd}_{1-x}\text{Mn}_x\text{S}$  [77–79]. This suggests that the mean field approximation leading to Eqs. (8) is not appropriate for the valence band of (Ga,Mn)As.

A breakdown of the mean field model occurs when the potential introduced by the Mn ions is comparable with the relevant bandwidth. We have calculated [68] the corrections to the mean field model by using a free-electron model with magnetic impurities described by square potentials. The calculation is based on the theory of Benoit à la Guillaume, Scalbert and Dietl, who computed the energy within the Wigner-Seitz approach [80].

The main result of the corrected theory is that the mean field approximation tends to underestimate the exchange coupling for low dilutions, as observed in our LSDA calculations. Our estimation of the exchange constant gives a value in the range of  $-4.9 \text{ eV} < N_0\beta < -4.4 \text{ eV}$ , which is very large if compared with the values quoted by experiments. Moreover it is very important to note that within this model the valence holes appear to be nearly bound to the Mn ions. This adds a further indication of the existence of the  $(3d^5 + h)$  complex, at least in the low dilution limit.

Finally we want to point out the fact that both the exchange constant and the valence band spin splitting are much larger than that found in typical experiments. There may be several reasons for this disagreement. First, there is strong experimental evidence in the absence of saturation in the  $M-H$  curves at large magnetic fields [81] and in recent X-ray magnetic dichroism measurements [75], that not all Mn ions contribute to the ferromagnetism. Of course an overestimation of  $x$  leads to an underestimation of  $N_0\beta$ . Second, the well-known lack of accuracy of the LDA to describe strongly localized charges may result in an overestimation of the p-d coupling [82]. This of course leads to a larger  $N_0\beta$  constant. However, we have shown that LDA does not strongly overbind the NiAs-type MnAs, and that the structural properties of zinc blende MnAs are very similar if calculated with LDA or LDA+U. This suggests that the error in the determination of the p-d coupling is not dramatic within LDA. Therefore we do believe that the two main conclusions from our LDA calculations, namely that the exchange constant is large enough for the mean field approximation to breakdown and that the holes are nearly bound, are indeed reliable. It is interesting to remark that in a recent paper [83] Chattopadhyay *et al.* found a  $T_c$  for (Ga,Mn)As in very good agreement with the experiments, by using dynamical mean field theory and our value for the exchange constant. Moreover the dynamical mean field theory estimation of the critical exchange constant needed for the formation of an impurity band agrees very well with our value [68]. This confirms the reliability of our analysis in the experimentally relevant regime.

## 5. THE IMPORTANCE OF INTRINSIC DEFECTS

So far we have always considered the ideal case in which only Mn ions are introduced in GaAs. If we assume the nominal valences for Mn ( $\text{Mn}^{2+}$ ) and Ga ( $\text{Ga}^{3+}$ ), we conclude that Mn acts as single acceptor in GaAs. Therefore an equal concentration of Mn ions and holes is expected. In contrast in the actual samples the hole concentration is much smaller than that of Mn [8] and some compensation mechanism occurs. As suggested in the first experimental works, the presence of As antisites  $\text{As}_{\text{Ga}}$ , usually quite abundant in low-temperature GaAs [84], is likely responsible for the compensation ( $\text{As}_{\text{Ga}}$  in GaAs is a double donor). Here we summarize the effect of  $\text{As}_{\text{Ga}}$  on the magnetic

properties of (Ga,Mn)As. The detailed results, obtained with SIESTA, can be found in Refs. [85–87].

### 5.1. Compensation Due to $\text{As}_{\text{Ga}}$ : Local Effects

We consider explicitly the effects of the inclusion of  $\text{As}_{\text{Ga}}$  in (Ga,Mn)As at different dilutions, and study how the chemical environment modifies the magnetic interaction between the Mn ions. We construct 64-(cubic) and 32-(rectangular) atom GaAs cells in which we include two Mn ions (leading to Mn concentrations of respectively  $x = 0.0625$  and  $x = 0.125$ ) and a variable number of  $\text{As}_{\text{Ga}}$  antisites. The parameter which quantifies the strength of the exchange coupling is the energy difference  $\Delta_{\text{FA}}$  between the total energies of the antiferromagnetic  $E_{\text{AF}}$  and ferromagnetic  $E_{\text{FM}}$  configurations of the supercell. These are obtained by fixing the spin direction at the beginning of the self-consistent calculation.

We further look at two possible spatial configurations of the Mn ions in the unit cell: (1) *separated*, when the Mn ions occupy positions as far apart as possible (i.e. the corner and the middle of the cubic cell), and (2) *close*, when the Mn atoms occupy two corners of a tetrahedron and are coordinated through a single As ion (see Fig. 7).

$\Delta_{\text{FA}}$  and  $M_{\text{Mn}}$  (the magnetization per Mn ion) for the *separated* arrangement are presented in Fig. 6 as a function of the number of  $\text{As}_{\text{Ga}}$  antisites. The magnetization per Mn ion is defined to be half of the magnetization of the cell, calculated in the FM-aligned phase. First we note that the ferromagnetic coupling is strongly weakened by  $\text{As}_{\text{Ga}}$  antisite doping. This is expected according to the picture of hole-mediated ferromagnetism:  $\text{As}_{\text{Ga}}$  antisites contribute electrons into the system and therefore compensate the holes.

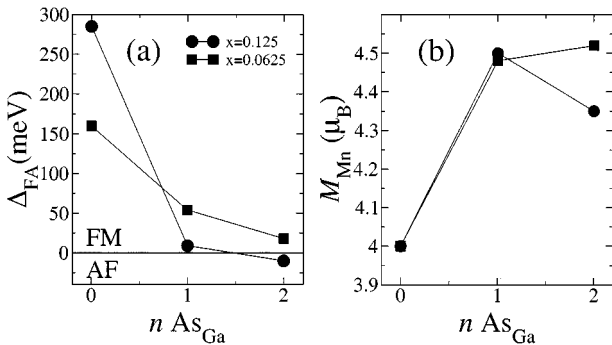


**Fig. 6.** (a) Energy difference between AF and FM alignments,  $\Delta_{\text{FA}}$ , and (b) magnetization per Mn ion,  $M_{\text{Mn}}$ , as a function of the number of  $\text{As}_{\text{Ga}}$  antisites in the cell: *separated* configuration. The horizontal line denotes the division between FM and AF alignment.

We also note that in the case of no antisites,  $\Delta_{\text{FA}}$  is much larger in the case of large Mn concentrations (we recall that according to Eq. (2)  $T_{\text{c}}$  scales linearly with  $x$ ). The figure also suggests that the compensation mechanism does not follow the nominal atomic valence, since a single  $\text{As}_{\text{Ga}}$  antisite per cell is not sufficient to destroy the ferromagnetic coupling. Above compensation (more than one  $\text{As}_{\text{Ga}}$  for two Mn ions) antiferromagnetic coupling is obtained for large Mn concentration, while the system stays ferromagnetic at low concentration, although in both cases  $\Delta_{\text{FA}}$  is rather small ( $|\Delta_{\text{FA}}| \leq 20$  meV). This is consistent with the onset of antiferromagnetic superexchange coupling [88], the mechanism which is believed to be responsible for the magnetic order in the II–VI DMS [76], at compensation. Super exchange is a short range interaction and therefore is less important in the low concentration limit where the Mn ions are well separated.

These results agree qualitatively with those obtained by Akai [72] for (In,Mn)As, using a KKR-CPA-LDA (Korringa–Kohn–Rostoker Coherent Potential Approximation and Local Density Approximation) method [89]. Akai interpreted his data as a competition between ferromagnetic double exchange and antiferromagnetic superexchange.

In Fig. 6b we see that  $M_{\text{Mn}}$  increases with the  $\text{As}_{\text{Ga}}$  concentration and then saturates to a value around  $4.5\mu_{\text{B}}$ . This can be easily explained by remembering that the top of the majority spin valence band of (Ga,Mn)As has some Mn d component due to hybridization (see Fig. 5).  $\text{As}_{\text{Ga}}$  doping moves the Fermi energy toward the conduction band, filling the valence band completely. This enhances the magnetic moment of the unit cell. The saturation is due to the fact that the next Mn d states available above the valence band are at the edge of the conduction band in the minority spin band. However  $\text{As}_{\text{Ga}}$  doping pins the Fermi energy at mid gap and these states cannot be filled. Note that a magnetic moment per Mn of  $4.5\mu_{\text{B}}$  is in good agreement with X-ray circular magnetic dichroism measurements [75].

A better insight into the mechanism giving rise to the ferromagnetic order is given by the results for the *close* configuration. In this case the local microscopic configuration is crucial for the magnetic properties; therefore we consider three different situations (see Fig. 7): (a) the antisites are far from the  $\text{Ga}_2\text{Mn}_2\text{As}_1$  complex, (b) one antisite occupies a tetrahedral site ( $\text{Ga}_1\text{Mn}_2\text{As}_2$ ), and (c) two antisites occupy the tetrahedral sites ( $\text{Mn}_2\text{As}_3$ ). The results for  $x = 0.0625$  are presented in Fig. 7.

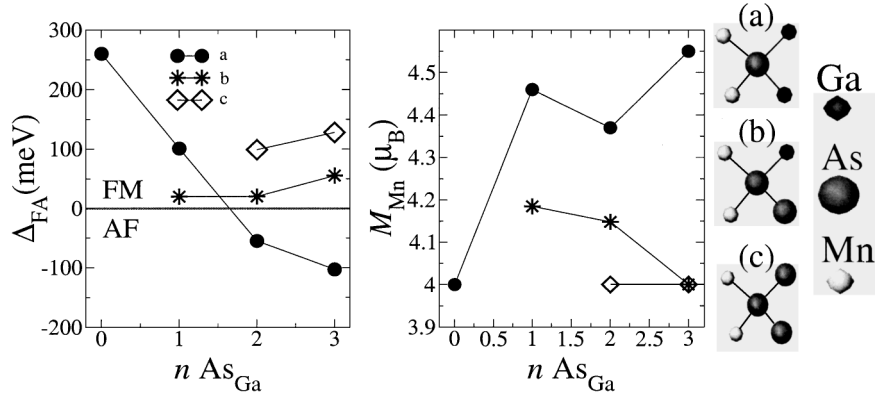


**Fig. 7.** Energy difference between the AF and FM alignments  $\Delta_{FA}$  (left), and magnetization per Mn ion  $M_{Mn}$  (right) as a function of the number of  $As_{Ga}$  antisites in the cell: *close* Mn arrangement. The symbols  $\bullet$ ,  $*$ , and  $\diamond$  represent arrangements (a), (b), and (c) respectively.

In case (a) both the  $\Delta_{FA}$  and  $M_{Mn}$  curves look very similar to those found for the *separated* arrangement (Fig. 6). The main difference is a strong antiferromagnetic coupling above compensation ( $n$   $As_{Ga} > 1$ ). Recalling that Mn in GaAs assumes the  $d^5$  configuration (d band half-filled), and that the Mn d shell is antiferromagnetically coupled with the intermediate As atom (through the p–d interaction), we conclude that superexchange coupling stabilizes the AF phase at and above compensation in the  $Ga_2Mn_2As_1$  complex. Note that the same conclusions have been drawn by Park *et al.* for  $Ge_{1-x}Mn_x$  [11], although in that case also the antiferromagnetic coupling seems to occur if holes are present.

Cases (b) and (c) present several interesting features. The most remarkable is that the ferromagnetic alignment is stable and almost insensitive to the total  $As_{Ga}$  concentration. This suggests that the dominant interaction in the  $Ga_1Mn_2As_2$  and  $Mn_2As_3$  complexes is completely local. Once again Mulliken population analyses help in understanding the electronic configuration of these complexes. In Table III we present the

Mulliken orbital population for the two Mn ions and the intermediate As ion of the complexes of Fig. 7. To understand the table, imagine the situation in which two  $As_{Ga}$  antisites are first located far from the Mn–As–Mn complex, and then each antisite is moved in turn to one of the two other corners of the tetrahedron. This corresponds to moving vertically (top to bottom) down the first half of the table. We notice that (i) the charge on the middle As atom increases, (ii) the spin-polarization of the p shell of the middle As atom increases, and (iii) the total population of the p shell of the middle As atom decreases. And most importantly the magnetic coupling changes from antiferromagnetic to ferromagnetic.

It is well known that in an antiferromagnetic crystal the presence of a bound carrier (electron or hole) which is Zener coupled to the local spins *always* induces a distortion in the antiferromagnetic lattice [90]. We therefore propose that the observed transition from antiferromagnetic in  $Ga_2Mn_2As_1$  to ferromagnetic coupling in  $Ga_1Mn_2As_2$  and  $Mn_2As_3$  results from the onset of ferromagnetic double-exchange coupling mediated by a bound Zener carrier. It is important to note that the potential necessary to bound an extra charge in the vicinity of the Mn ions is provided by the As antisites. We also emphasize that if  $Ga_2Mn_2As_1$  or  $Mn_2As_3$  complexes are present in actual samples, then the Mn ions in the complexes will not contribute to the overall ferromagnetic alignment, being magnetically “locked” by the local environment. This is a possible explanation of the fact that in actual samples only a fraction of the Mn ions contribute to the ferromagnetism [75,81]. Similar conclusions based on DFT calculations have been drawn for  $Ge_{1-x}Mn_x$  [11].

**Table III.** Mulliken Atomic and Orbital Populations for the Mn Ions and the Intermediate As Atom of the Complexes of Fig. 7<sup>a</sup>

$n$ $As_{Ga}$	Type	Mn- $d_{\uparrow}$	Mn- $d_{\downarrow}$	As- $p_{\uparrow}$	As- $p_{\downarrow}$	As-p	As
2	a	4.74	0.70	1.55	1.63	3.18	4.92
2	b	4.74	0.71	1.50	1.67	3.17	4.95
2	c	4.72	0.75	1.44	1.71	3.15	4.97
3	a	4.76	0.68	1.57	1.63	3.20	4.93
3	b	4.74	0.74	1.55	1.65	3.20	4.97
3	c	4.73	0.75	1.49	1.69	3.17	4.99

<sup>a</sup>The Mn concentration is  $x = 0.0625$ . The symbols  $\uparrow$  and  $\downarrow$  correspond to majority and minority spin respectively. The populations are in units of the electronic charge  $|e|$ .

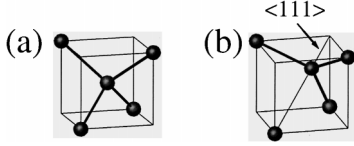


**Fig. 8.** (a)  $\text{As}_{\text{Ga}}$  and (b)  $\text{As}_i\text{-V}_{\text{Ga}}$  pair obtained by moving  $\text{As}_{\text{Ga}}$  along the  $\langle 111 \rangle$  direction.

## 5.2. Defect Manipulation

In a recent paper [86] we have shown that intrinsic defect manipulation can provide a valuable way of tuning the carrier concentration and hence enhancing the  $T_c$  in (Ga,Mn)As, without changing the Mn concentration nor the microscopic configuration of the Mn ions. Here we summarize the basic ideas. We first recall that isolated  $\text{As}_{\text{Ga}}$  in GaAs are responsible for the photoquenchable EL2 defect [91]. In fact upon illumination,  $\text{As}_{\text{Ga}}$  undergoes a structural transition to an As interstitial–Ga vacancy ( $\text{As}_i\text{-V}_{\text{Ga}}$ ) pair, which is obtained by moving  $\text{As}_{\text{Ga}}$  along the  $\langle 111 \rangle$  direction (see Fig. 8). This complex is metastable since  $\text{As}_{\text{Ga}}$  can be regenerated by heating. It is crucial to observe that the  $\text{As}_i\text{-V}_{\text{Ga}}$  pair is not electronically active in GaAs, since its only state in the band gap is completely filled. In what follows we show that this metastable complex is present, can be obtained by illumination, and is also electronically inactive in (Ga,Mn)As.

In Fig. 9 we present the total energy and the magnetization of a 64-atom unit cell containing one Mn ion ( $x = 0.03125$ ) and one  $\text{As}_{\text{Ga}}$  (note that in this case the system is n doped, with one excess electron per unit cell) as a function of the displacement  $l_{\langle 111 \rangle}$  of  $\text{As}_{\text{Ga}}$  along  $\langle 111 \rangle$ . For comparison we also present the

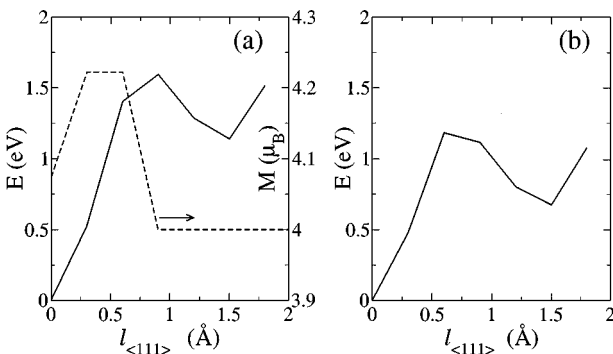


**Fig. 9.** Total energy (left-hand-side scale) and magnetization (right-hand-side scale) for (a) (Ga,Mn)As and (b) GaAs as a function of the displacement of an  $\text{As}_{\text{Ga}}$  antisite along  $\langle 111 \rangle$ . The energy of  $l_{\langle 111 \rangle} = 0$  is set to 0 eV.

same curve for GaAs, which is in very good agreement with previously published results [91]. It is clear that in (Ga,Mn)As also the  $\text{As}_i\text{-V}_{\text{Ga}}$  defect is metastable and that the energy barrier for the thermal regeneration is 0.45 eV. This, according to kinetic calculations [91], gives a regeneration temperature of about 100 K.

Having established that the  $\text{As}_i\text{-V}_{\text{Ga}}$  defect is metastable let us now prove that it can also be generated in (Ga,Mn)As. The mechanism has been explained by Scheffler *et al.* [91,92], and can be summarized as follows. It is known that the excited  $a_1^1t_2^1$  electronic configuration of a tetrahedral substitutional double donor induces lattice distortion. Such distortion occurs in  $\text{As}_{\text{Ga}}$ , which possesses a doubly occupied donor level  $a$  at midgap and an empty resonant state with  $t_2$  symmetry close to the conduction band edge. The distortion is initiated because the many-electron wave function of the  $a_1^1t_2^1$  configuration is orbitally degenerate and therefore the system is Jahn–Teller unstable. Jahn–Teller distortion splits the  $t_2$  state into a lower  $a$  state (half-filled) and a higher  $e$  state (empty). Therefore an optical excitation of the  $a_1^2t_2^0$  ground state to the  $a_1^1t_2^1$  will initiate a distortion. It has been demonstrated that in GaAs the total-energy curve as a function of the displacement of  $\text{As}_{\text{Ga}}$  along  $\langle 111 \rangle$  for the  $a_1^1t_2^1$  configuration has a minimum for  $l_{\langle 111 \rangle} \sim 0.3 \text{ \AA}$  [91]. Then the system has some probability of relaxing onto the  $\text{As}_i\text{-V}_{\text{Ga}}$  side of the total-energy curve of Fig. 9, ending up considerably far from the antisite position, creating the  $\text{As}_i\text{-V}_{\text{Ga}}$  pair.

The same mechanism holds for (Ga,Mn)As since the only difference with respect to GaAs is the spin splitting of the bands. This splitting, however, does not move the  $a$  state of  $\text{As}_{\text{Ga}}$  into the valence band nor the  $t_2$  state into the conduction band. With these considerations it is clear that the As antisite in (Ga,Mn)As presents the same features as that in GaAs and, therefore, the mechanism described above is still applicable.

The effects of this transition on the ferromagnetic properties are quite dramatic. We calculate the energy difference between the ferromagnetic and antiferromagnetic alignment,  $\Delta_{\text{FA}}$ , and we observe an increase from 53 to 124 meV when a single  $\text{As}_{\text{Ga}}$  is transformed into a  $\text{As}_i\text{-V}_{\text{Ga}}$  pair. Hence the ferromagnetic order is strengthened. The reason for this enhancement of the ferromagnetic coupling is that most of the hole compensation introduced by  $\text{As}_{\text{Ga}}$  is lifted by the creation of the  $\text{As}_i\text{-V}_{\text{Ga}}$  pair. The band structures of (Ga,Mn)As containing  $\text{As}_{\text{Ga}}$  and  $\text{As}_i\text{-V}_{\text{Ga}}$  pair shown

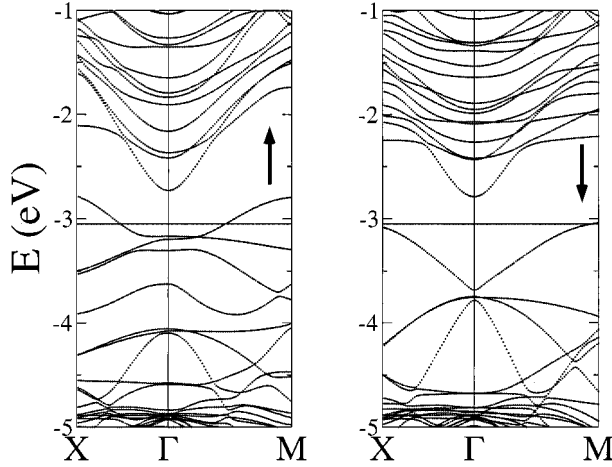


**Fig. 10.** Band structure for  $\text{Ga}_{1-x}\text{Mn}_x\text{As}$  with intrinsic defects:  $\text{As}_{\text{Ga}}$ . These are the bands for a cubic 64-atom supercell ( $2 \times 2 \times 2$  zinc blende cubic cells) containing one Mn ion and one  $\text{As}_{\text{Ga}}$ . On the right-hand side the majority spin and on the left the minority. The horizontal line denotes the position of the Fermi energy.

in Figs. 10 and 11 explain this point. It is clear that in the case of  $\text{As}_{\text{Ga}}$  the Fermi energy cuts through the  $\text{As}_{\text{Ga}}$  impurity band, leaving the GaAs valence band completely filled (note that the donor level is only marginally spin-split, although it is hybridized with the top of the valence band). This means that the compensation is complete (note that in the figure we have one Mn ion and one  $\text{As}_{\text{Ga}}$  in the cell; therefore we correctly expect an excess of one electron in the impurity

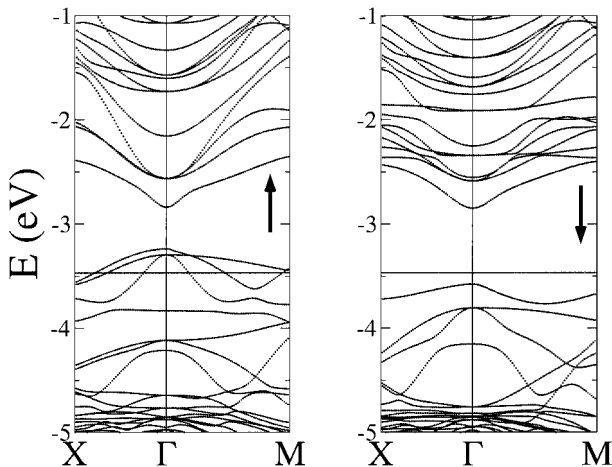


**Fig. 11.** Band structure for  $\text{Ga}_{1-x}\text{Mn}_x\text{As}$  with intrinsic defects:  $\text{As}_i\text{-V}_{\text{Ga}}$  pair. These are the bands for a cubic 64-atom supercell ( $2 \times 2 \times 2$  zinc blende cubic cells) containing one Mn ion and one  $\text{As}_i\text{-V}_{\text{Ga}}$  pair. On the right-hand side the majority spin and on the left the minority. The horizontal line denotes the position of the Fermi energy.

band). In contrast, in the case of the  $\text{As}_i\text{-V}_{\text{Ga}}$  pair there are still holes in the system, since the Fermi energy cuts through the top of the valence band and the impurity level. It is also important to note that the impurity level has small hybridization with the majority valence band of  $(\text{Ga},\text{Mn})\text{As}$ . This means that in this case there are holes in the system with a dispersion very close to that of the defect-free case. For this reason the presence of  $\text{As}_i\text{-V}_{\text{Ga}}$  pairs does not alter the magnetic properties compared with the defect-free alloy (note that  $\Delta_{\text{FA}}$  for this situation is 124 meV, very similar to the defect-free value of 159 meV).

In conclusion, the optically induced transition of  $\text{As}_{\text{Ga}}$  to a  $\text{As}_i\text{-V}_{\text{Ga}}$  pair reduces the hole compensation, strengthening the ferromagnetic coupling. This, in principle, allows tuning of the hole concentration without acting on the chemical composition of a sample. However, since the antisites regenerate for temperatures of the order of 100 K, the mechanism cannot be used to obtain very high  $T_c$ 's.

## 6. DILUTED FERROMAGNETIC HETEROSTRUCTURES: MAGNETIC AND TRANSPORT PROPERTIES

We have seen in the previous sections that formation of the NiAs-type phase of MnAs is easier than formation of the zinc blende phase, which in turn is very desirable because of its half-metallic band structure. It has been demonstrated [32], however, that zinc blende MnAs can be grown up to half of a monolayer in GaAs/MnAs superlattices. These structures are called digital ferromagnetic heterostructures (DFH). Since our earlier work has shown a strong dependence of the magnetic properties on the local arrangement of the Mn ions, we expect that the properties of DFHs would be very different from their random alloy counterparts.

These are the main experimental findings [32]: first,  $T_c$  decays with increasing GaAs layer thickness separating the MnAs sub-monolayers, and saturates for thicknesses larger than  $\sim 50$  GaAs monolayers. The saturation is unexpected according to the mean field model for three-dimensional systems, since the total Mn concentration in the sample decreases with the increase of the GaAs thickness. This separation dependence suggests that DFHs behave like planar systems.

Second, Hall measurements in the direction parallel to the MnAs planes show an anomalous Hall effect for undoped samples, which disappears upon Be doping [93,94]. Large Shubnikov de Haas oscillations

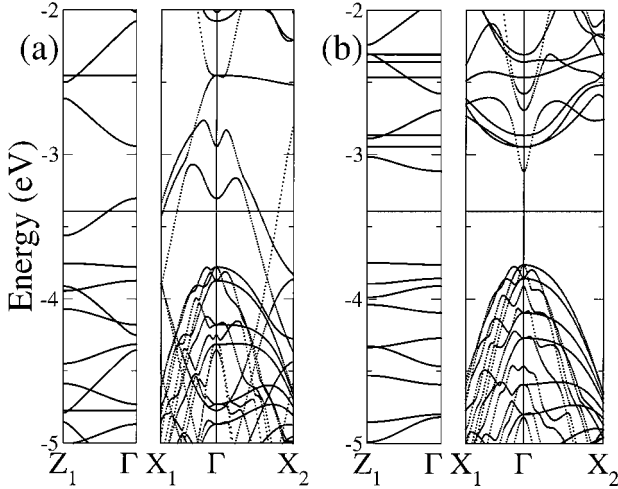


**Fig. 12.** Band structure for a  $\text{MnAs}_1/\text{GaAs}_{15}$  superlattice: (a) majority and (b) minority spins.  $X_1$  and  $X_2$  are in the MnAs plane and denote directions along respectively the edge and the diagonal of the cubic supercell.  $\Gamma \rightarrow Z_1$  is the direction orthogonal to the MnAs plane. The horizontal line indicates the Fermi energy.

are found in doped samples, although surprisingly the charge densities extracted from the Hall coefficient and from the Shubnikov de Haas oscillations are different. This suggests that two different carrier types could be present in the system.

Density functional theory has answered the following questions regarding the physics of DFHs: (i) what is the real dimensionality of the system? (ii) are the carriers spin polarized? (iii) what is the carrier distribution in the system?

We have used the code SIESTA [95] with a DFH superlattice constructed from  $N$  GaAs cubic cells (eight atoms in the cell) aligned along the  $z$  direction. One Ga plane (two atoms) is substituted with Mn and periodic boundary conditions are applied. This leads to an infinite  $\text{MnAs}_1/\text{GaAs}_{2N-1}$  superlattice, where MnAs zinc blende monolayers are separated by a  $5.65 \times N \text{ \AA}$  thick GaAs layer. In Fig. 12 we present the calculated band structure for the case  $N = 8$  (with a  $45.2 \text{ \AA}$  thick GaAs interlayer), for both the majority and minority spins. It shows clearly a very peculiar half-metallic structure. Although the band structure has a gap for the minority spin and some band crossing at the Fermi energy for the majority, the band dispersion in the MnAs plane ( $X_1 \rightarrow \Gamma \rightarrow X_2$ ) is quite broad while the one perpendicular to the MnAs plane ( $Z_1 \rightarrow \Gamma$ ) is very narrow (impurity-like band). Therefore MnAs/GaAs looks like a *two-dimensional* half-metal with small hopping between the MnAs planes.

We also look at the stability of the ferromagnetic phase as a function of the separation between Mn planes, by calculating  $\Delta_{\text{FA}}$ . Surprisingly  $\Delta_{\text{FA}}$  is independent of the GaAs thickness for the range of thicknesses investigated here (531, 533, and 515 meV respectively for  $N = 4$ ,  $N = 6$ , and  $N = 8$ ). This is consistent with the experimental insensitivity of  $T_c$  to the GaAs thickness. This first analysis shows that most of the physics of DFH occurs in the MnAs planes.

In order to have a better understanding we have also performed transport calculations in the ballistic limit. One of the advantages of using a localized basis set for the DFT calculation is that at the end of the self-consistent procedure a tight-binding Hamiltonian is generated by direct numerical integration over a real space grid [53]. Then transport properties can be calculated in the ballistic limit by using a well-established technique for tight-binding Hamiltonians, which is described in Ref. [96]. For this work, we have generalized the technique to the case of nonorthogonal tight-binding models with singular coupling matrices [95]. More details can be found in the cited literature.

In Fig. 13 we present our calculated conductance per unit area as a function of the position of the Fermi energy for an  $\text{MnAs}_1/\text{GaAs}_{15}$  superlattice for both the current in the MnAs plane (CIP) and the current perpendicular to the Mn plane (CPP) directions, and for both spins. We also project the conductance onto the atomic orbital basis set in order to determine the orbital character of the electrons carrying

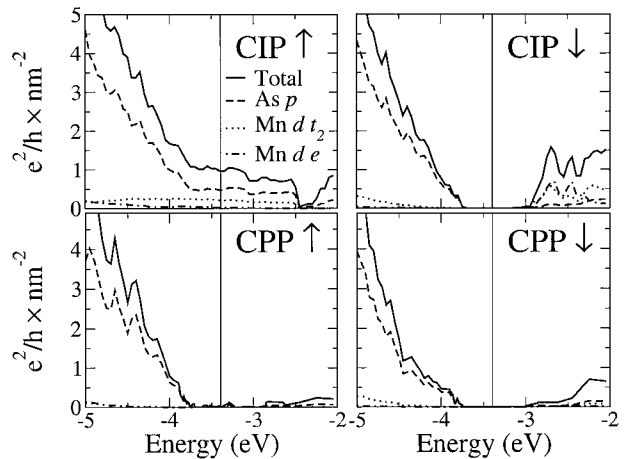


**Fig. 13.** Total and partial conductance per unit area for a  $\text{MnAs}_1/\text{GaAs}_{15}$  superlattice as a function of the position of the Fermi energy for majority ( $\uparrow$ ) and minority ( $\downarrow$ ) spin bands. The vertical line denotes the position of the Fermi energy for undoped samples.

the current [96]. As expected from the band structure, the ballistic current is 100% spin polarized, with no current for the minority spin band. In the majority spin band the behavior is very different for the CIP and CPP alignment. In the CIP case the conductance is quite large and independent of the energy, with a significant contribution (roughly 20% of the total conductance) coming from the Mn  $d_{t_2}$  orbitals. In contrast, the conductance is very small in the CPP direction, with orbital contribution almost entirely from the As  $p$  states. Moreover the conductance at  $E_F$  comes from just a few  $k$ -points around the  $\Gamma$  point (in the direction orthogonal to the transport). These correspond to the states with the largest kinetic energy in the direction of the transport. This situation is similar to that occurring in tunneling junctions and so we describe the transport as tunneling-like, meaning that the transport in the CPP direction is through hopping between the MnAs planes.

Finally we investigate the spatial distribution of the current. This is given by the charge density distribution in real space,  $\rho(\mathbf{r})$ , calculated only for those states contributing to the conductance (see Fig. 14) [95]. The figure confirms that the current in the CIP case is distributed mainly in a narrow region around the MnAs planes, with small spillage outside. In contrast, the CPP current is mainly located at the Mn plane with small contributions from the GaAs layers. This means that carriers are strongly confined in the

MnAs plane and the perpendicular transport is via hopping between the planes.

DFT has therefore answered all the questions stated at the beginning of this section. The DFHs appear to be two-dimensional half-metals, with a metallic-like ballistic conductance in the MnAs plane and an hopping conductance perpendicular to the MnAs planes. The ferromagnetism is therefore insensitive to the GaAs layer thickness, showing no dilution effect.

## 7. OTHER DILUTED MAGNETIC SEMICONDUCTORS

So far we have concentrated primarily on the properties of (Ga,Mn)As, which is the most well studied of the DMSs. However, in the last year several other DMSs have been synthesized, some of them showing remarkably high  $T_c$ . At the same time several DFT calculations have been published both explaining the properties of existing materials or making predictions for new ones. The prediction of material properties in advance of experiments is one of the most important aspects of density functional theory. Here we review the principal works in this area.

### 7.1. $\text{Ga}_{1-x}\text{M}_x\text{As}$ with $\text{M} = \text{V}, \text{Cr}, \text{Fe}$

Doping of GaAs with transition metals other than Mn has been investigated theoretically using both the full-potential linearized augmented plane wave (FLAPW) method [61] and the atomic sphere approximation [70]. Since the first method is computationally more demanding the author concentrates on the electronic structure of hypothetical zinc blende MAs with  $\text{M} = \text{V}, \text{Cr}, \text{Mn}, \text{Fe}$ , and on the high concentration limit of  $\text{Ga}_{1-x}\text{M}_x\text{As}$  ( $x = 0.25$  and  $x = 0.125$ ). The main result is that while the ground state of FeAs is antiferromagnetic, VAs, CrAs, and MnAs at the respective equilibrium lattice constants appear to be half-metallic ferromagnets with magnetic moments respectively of  $2\mu_B$ ,  $3\mu_B$ , and  $4\mu_B$  per formula unit.

Turning attention to  $\text{Ga}_{1-x}\text{M}_x\text{As}$  it is interesting to note that the calculated DOS for  $\text{Ga}_{1-x}\text{V}_x\text{As}$  in the large concentration limit reveals very small hybridization of the V 3d orbitals with the GaAs valence band, suggesting that in this compound the magnetic coupling may be rather small. In contrast,  $\text{Ga}_{1-x}\text{Cr}_x\text{As}$  shows a DOS very similar to that of  $\text{Ga}_{1-x}\text{Mn}_x\text{As}$ . This suggests that  $\text{Ga}_{1-x}\text{Cr}_x\text{As}$

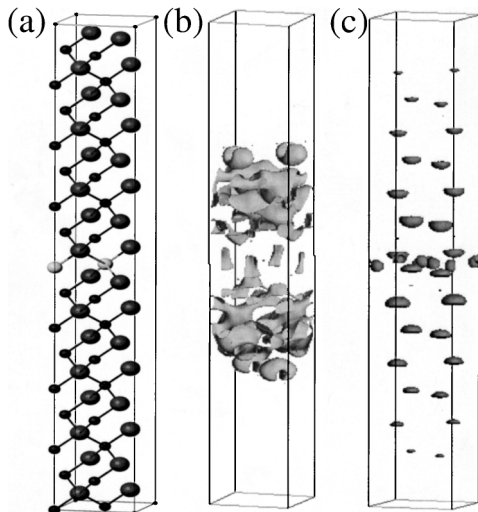


**Fig. 14.** Charge density distribution in real space for  $\text{MnAs}_1/\text{GaAs}_{15}$  (a) calculated only for those states contributing to the conductance and energy within 0.3 eV from  $E_F$ : CIP (b) and CPP (c) configurations.

may be a potential candidate for a high  $T_c$  DMS. In addition van Schilfhaarde and Mryasov fit their DFT results with a pairwise Heisenberg-like energy  $E = -\sum_{ij} J_{ij} \vec{s}_i \cdot \vec{s}_j$ , and found that the values of  $J$  for  $\text{Ga}_{1-x}\text{Cr}_x\text{As}$  are larger than those of  $\text{Ga}_{1-x}\text{Mn}_x\text{As}$ . This suggests stronger ferromagnetism for  $\text{Ga}_{1-x}\text{Cr}_x\text{As}$  than for  $\text{Ga}_{1-x}\text{Mn}_x\text{As}$ . However this prediction is strongly affected by the fact that the DFT results strongly deviate from the Heisenberg-like form.

Experimentally both  $\text{Ga}_{1-x}\text{Fe}_x\text{As}$  [97] and  $\text{Ga}_{1-x}\text{Cr}_x\text{As}$  [98] have been synthesized and there is a little evidence for ferromagnetic order. However very recently zinc blende CrAs has been successfully grown on GaAs at low temperature [99], showing a  $T_c$  above room temperature. Moreover preliminary measurements show a magnetic moment per formula unit very close to  $3\mu_B$ , in good agreement with the theoretical predictions [61]. To our knowledge  $\text{Ga}_{1-x}\text{V}_x\text{As}$  has never been grown.

## 7.2. $\text{Ga}_{1-x}\text{Mn}_x\text{N}$

There has been a large effort in synthesizing  $\text{Ga}_{1-x}\text{Mn}_x\text{N}$  in the last two years, since Dietl *et al.* predicted a Curie temperature higher than any other Mn-doped semiconductors for this compound [17]. Very recently this prediction has been confirmed experimentally [10], with  $\text{Ga}_{1-x}\text{Mn}_x\text{N}$  at 10% Mn concentration showing a remarkably large  $T_c$  (940 K). Unfortunately the mechanism for the ferromagnetism in  $\text{Ga}_{1-x}\text{Mn}_x\text{N}$  is not clearly understood because of the lack of experimental data. In particular the nature and the role of the free carriers (if present) are not yet clear.

Sato and Katayama-Yoshida performed DFT calculations within the KKR-CPA method [100]. They looked at transition-metal doping of GaN and studied the stability of the ferromagnetic configuration against the spin glass state. The ferromagnetic state appears to be stable for (Ga,V)N and (Ga,Cr)N, while for (Ga,Fe)N, (Ga,Co)N, and (Ga,Ni)N the spin glass state has lower total energy at every concentrations studied ( $x = 0.05, 0.1, 0.15, 0.20, 0.25$ ). The case of (Ga,Mn)N is critical since the ferromagnetic state is stable only at low Mn concentration ( $x < 0.15$ ). This is explained in terms of competition between double exchange and superexchange, with the latter being dominant for small Mn–Mn separations.

The DOS of (Ga,Mn)N looks rather different than that of (Ga,Mn)As, showing a much stronger

d contribution at the Fermi energy and smaller p–d hybridization. This leads to the formation of an Mn d impurity band in the band gap of GaN, as calculated by Kronik *et al.* [101], who also calculated that the (Ga,Mn)N valence band is not spin split. The atomic configuration of Mn is calculated to be  $\text{Mn}^{3+}$  with the d orbitals arranging as  $d^4$  [100]. This contradicts the experimental results for paramagnetic (Ga,Mn)As [102], which convincingly show a  $d^5$  ( $S = 5/2$ ) configuration. The reasons of this discrepancy are not clear at the moment.

## 7.3. $\text{Zn}_{1-x}\text{M}_x\text{O}$ with $\text{M} = \text{V, Cr, Mn, Fe, Co, Ni}$

The mean field model of Dietl *et al.* also predicts a very large  $T_c$  for Mn-doped ZnO [17], provided that the sample is p doped. Sato and Katayama-Yoshida also investigated the stability of the ferromagnetic phase with respect to the spin glass phase for  $\text{Zn}_{1-x}\text{M}_x\text{O}$  ( $\text{M} = \text{V, Cr, Mn, Fe, Co, Ni}$ ), again using a KKR-CPA method [103–105]. They found a ferromagnetic ground state for all the materials except Mn, for which the spin glass configuration has a lower energy. However they also showed that in the case of Mn the ferromagnetic configuration can be obtained by large p doping (they substitute N atoms at the O sites in their calculations).

Since in the II–VI semiconductors only very small hole concentrations can be obtained by doping, they also investigated the conditions to have strong ferromagnetism in transition-metal-doped ZnO with additional n doping (Ga at the Zn sites). The result of this calculation is that the presence of electrons stabilizes the ferromagnetic order in ZnO doped with Fe, Co, and Ni [104]. It is important to note that in all these cases the Mn d shell is more than half-filled and that the Fermi energy is located within an Mn d region of the minority spin density of states. These are the conditions for strong double-exchange coupling between the transition-metal ions. The fact that n-doped (Zn,Co)O [14] and (Zn,Ni)O [106] have been grown, showing  $T_c$ 's above room temperature, is very encouraging.

Similar calculations have been carried out for transition-metal-doped ZnS, ZnSe, and ZnTe [107,108] without any additional doping. These show that only V- and Cr-doped materials have a ferromagnetic ground state, which is due to double-exchange coupling. In this case the carriers mediating the double exchange are holes at the top of the valence band, which in turn are strongly hybridized

with the p states of the group VI element. It is worth mentioning that to date no ferromagnetic order has been found experimentally in these materials. However real samples present strong self-compensation, which suppresses the hole-mediated double-exchange mechanism.

#### 7.4. $M_{1-x}Mn_xGeP_2$ with $M = Cd, Zn$ and $II = P, As$

$Cd_{1-x}Mn_xGeP_2$  was the first room temperature diluted ferromagnetic semiconductors to be grown [12]. It has a body-centered tetragonal cell, and the main advantage of this structure is that Mn can substitute for the II cations, adopting the  $Mn^{2+}$  state (“natural” for Mn). Accurate calculations with both GGA and LDA have been performed [109,110], showing that indeed Mn assumes an  $Mn^{2+}$  state. The calculations demonstrate a very weak sensitivity of the magnetic and electronic structure on both the anion (As or P) and cation (Cd or Zn) elements.

Interestingly both the LDA and GGA results give an antiferromagnetic ground state, contradicting the experimental results. However two aspects must be pointed out. First, the samples in the experiments [12] are prepared with vacuum deposition on a single crystal surface, followed by solid-state reaction at high temperature. This means that most of the Mn ions are located close to the surface. The DFT calculations are performed for perfect crystalline bulk systems, whose properties will certainly differ from those of the actual samples. Second, it has been demonstrated [110] that the ferromagnetic phase can become stable against the antiferromagnetic one, if electrons are introduced in the system (S substituting for P). This seems to suggest that the presence of free carriers is also essential for ferromagnetic order in chalcopyrite semiconductors.

Finally, very recently Mahadevan and Zunger calculated the formation energies of several intrinsic defects of  $CdGeP_2$ , of Mn impurities in  $CdGeP_2$  either at the Cd or at the Ge site, and of complexes of these [111]. They found that under Cd-, Mn-, and P-rich growth conditions,  $Mn_{Ge}$  impurities naturally form in the crystal. These impurities, that in contrast to Mn in GaAs do not form clusters, are acceptors in  $CdGeP_2$  and align ferromagnetically. In addition it is important to observe that the ferromagnetic coupling is also found between  $Mn_{Ge}$  and  $Mn_{Cd}$  impurities. These predictions offer very good guidelines for growing room-temperature Mn-doped  $CdGeP_2$ .

## 8. CONCLUSIONS AND FUTURE DIRECTIONS

In this paper we have presented the recent DFT contributions to the physics of diluted magnetic semiconductors. Most of the results are for (Ga,Mn)As, have been obtained within either the LSDA or the GGA approximation, and capture most of the relevant physics of (Ga,Mn)As. We have also summarize the latest results for other DMSs, whose properties are less well studied and understood.

During these studies several disagreements with experiments have appeared, suggesting that in some cases the LSDA/GGA approximations may be not completely appropriate. It is therefore indispensable to understand the limit of the reliability of the LSDA/GGA approximations and eventually to correct them. It is well known that the local density approximation fails in describing systems where electron–electron interaction is strong. This generally happens when we try to describe orbitals tightly bound to their nuclei. The d orbitals of transition metals in transition-metal oxides are an example of this.

A typical signature of the inappropriateness of the LSDA/GGA is that the bands from tightly bound orbitals are pushed toward higher energies. This can create the following problems in DMSs: (1) underestimation of the true band occupation, leading to an erroneous magnetic moment, (2) overestimation of p–d interaction, due to artificially strong hybridization, (3) overbinding of the structure, (4) tendency to metallicity in otherwise semiconducting systems, and (5) prediction of the wrong magnetic state (i.e. ferromagnetic instead of antiferromagnetic). All these problems can of course strongly affect the predictions of DFT calculations, and they must be corrected.

Several schemes have been adopted to go beyond the LSDA/GGA approximation, and here we briefly list them. In 1981 Perdew and Zunger [44] showed that most of the problems of the LDA approximation come from its incorrect treatment of coulombic self-interaction. They demonstrated that self-interaction corrections, namely the subtraction of spurious self-interaction from the density functional, greatly improve the description of localized states. Since then several implementations have been made [112] including algorithms using pseudopotentials [113].

A quite different approach to this problem is represented by the LDA+U scheme [42,43]. The main idea is to combine density functional theory with an Hubbard description of those orbitals which suffer strong correlations. In this case an additional

Hubbard-like term is added to the energy functional and the consequent single-particle equations are deduced. The theory gain two extra parameters (the Hubbard parameter  $U$  and the Hund's rule exchange  $J$ ), which can be fixed from experimental values or calculated self-consistently. The advantages of the LDA+U scheme are the relatively easy numerical implementation and the fact that the parameters can be directly compared with those coming from simpler models.

In conclusion, we have shown that DFT can be a very powerful tool for describing structural, electronic, magnetic, and transport properties of diluted magnetic semiconductors. In particular DFT is very useful for obtaining parameters not accessible from experiments, and for providing accurate descriptions of properties occurring at the atomic scale. The prediction of new materials with novel properties is possible, although special care should be taken in order to keep errors coming from the local density approximation under control.

## ACKNOWLEDGMENTS

We thank S. Picozzi, L. Kronik, S. Hellberg, P. Mahadevan, and B. I. Min for useful discussions, comments, and permission to discuss unpublished results. This work made use of MRL Central Facilities supported by the National Science Foundation under award No. DMR96-32716. This work is supported by ONR Grant N00014-00-10557, by NSF-DMR under the Grant 9973076, and by ACS PRF under the Grant 33851-G5.

## REFERENCES

- G. Prinz, *Science* **282**, 1660 (1998); G. Prinz, *Phys. Today* **48**, 58 (1995).
- M. N. Baibich, J. M. Broto, A. Fert, F. Nguyen Van Dau, F. Petroff, P. Etienne, G. Creuzet, A. Friederich, and J. Chazelas, *Phys. Rev. Lett.* **61**, 2472 (1988); G. Binasch, P. Grünberg, F. Sauerbach, and W. Zinn, *Phys. Rev. B* **39**, 4828 (1989).
- H. X. Tang, F. G. Monzon, R. Lifshitz, M. C. Cross, and M. L. Roukes, *Phys. Rev. B* **61**, 4437 (2000), and references therein.
- W. Y. Lee, S. Gardelis, B. C. Choi, Y. B. Xu, C. G. Schmidt, C. H. W. Barnes, D. A. Ritchie, E. H. Linfield, and J. A. C. Bland, *Appl. Phys. Lett.* **85**, 6682 (1999).
- P. R. Hammar, B. R. Bennet, M. J. Yang, and M. Johnson, *Phys. Rev. Lett.* **83**, 203 (1999).
- G. Schmidt, D. Ferrand, L. W. Molenkamp, A. T. Filip, and B. J. van Wees, *Phys. Rev. B* **62**, R4790 (2000).
- P. R. Hammar and M. Johnson, *Appl. Phys. Lett.* **79**, 2591 (2001).
- H. Ohno, *J. Magn. Magn. Mater* **200**, 110 (1999); H. Ohno, *Science* **281**, 951 (1998).
- H. Ohno, H. Munekata, T. Penney, S. von Molnar, and L. L. Chang, *Phys. Rev. Lett.* **68**, 2664 (1992).
- S. Sonoda, S. Shimizu, T. Sasaki, Y. Yamamoto, and H. Hori, cond-mat/0108159.
- Y. D. Park, A. T. Hanbicki, S. C. Erwin, C. S. Hellberg, J. M. Sullivan, J. E. Mattson, T. F. Ambrose, A. Wilson, G. Spanos, and B. T. Jonker, preprint.
- G. A. Medvedkin, T. Ishibashi, T. Nishi, K. Hayata, Y. Hasegawa, and K. Sato, *Jpn. J. Appl. Phys.* **39**, L949 (2000).
- Y. Matsumoto, M. Murakami, T. Shono, T. Hasegawa, T. Fukumura, M. Kawasaki, P. Ahmet, T. Chikyow, S.-Ya. Koshihara, and H. Koinuma, *Science* **291**, 854 (2001).
- K. Ueda, H. Tabata, and T. Kawai, *Appl. Phys. Lett.* **79**, 988 (2001).
- Y. Ohno, D. K. Young, B. Beschoten, F. Matsukura, H. Ohno, and D. D. Awschalom, *Nature* **402**, 790 (1999).
- H. Ohno, D. Chiba, F. Matsukura, T. Omiya, E. Abe, T. Dietl, Y. Ohno, and K. Ohtani, *Nature* **408**, 944 (2000).
- T. Dietl, H. Ohno, F. Matsukura, J. Cibert, and D. Ferrand, *Science* **287**, 1019 (2000); T. Dietl, H. Ohno, and F. Matsukura, *Phys. Rev. B* **63**, 195205 (2001).
- T. Jungwirth, W. A. Atkinson, B. H. Lee, and A. H. MacDonald, *Phys. Rev. B* **59**, 9818 (1999).
- J. Szczytko, W. Mac, A. Stachow, A. Twardowski, P. Becla, and J. Tworzydło, *Solid State Commun.* **99**, 927 (1996).
- K. Ando, T. Hayashi, M. Tanaka, and A. Twardowski, *J. Appl. Phys.* **83**, 6548 (1998).
- J. Szczytko, W. Mac, A. Twardowski, F. Matsukura, and H. Ohno, *Phys. Rev. B* **59**, 12935 (1999).
- F. Matsukura, H. Ohno, A. Shen, and Y. Sugawara, *Phys. Rev. B* **57**, R2037 (1998).
- T. Omiya, F. Matsukura, T. Dietl, Y. Ohno, T. Sakon, M. Motokawa, and H. Ohno, *Physica E* **7**, 976 (2000).
- J. Okabayashi, A. Kimura, O. Rader, T. Mizokawa, A. Fujimori, T. Hayashi, and M. Tanaka, *Phys. Rev. B* **58**, R4211 (1998).
- T. Hayashi, Y. Hashimoto, S. Katsumoto, and Y. Iye, *Appl. Phys. Lett.* **78**, 1691 (2001).
- S. J. Potashnik, K. C. Ku, S. H. Chun, J. J. Berry, N. Samarth, and P. Schiffer, *Appl. Phys. Lett.* **79**, 1495 (2001).
- H. Hohenberg and W. Kohn, *Phys. Rev.* **136**, B864 (1964).
- W. Kohn and L. J. Sham, *Phys. Rev.* **140**, A1133 (1965).
- G. B. Bachelet, D. R. Hamann, and M. Schlüter, *Phys. Rev. B* **26**, 4199 (1982).
- O. F. Sankey and D. J. Niklewski, *Phys. Rev. B* **40**, 3979 (1989).
- P. Ordejón, *Phys. Stat. Sol. B* **217**, 335 (2000).
- R. K. Kawakami, E. Johnston-Halperin, L. F. Chen, M. Hanson, N. Guébels, J. S. Speck, A. C. Gossard, and D. D. Awschalom, *Appl. Phys. Lett.* **77**, 2379 (2000).
- M. T. Yin and M. L. Cohen, *Phys. Rev. B* **26**, 5668 (1982).
- J. Neugebauer and M. Scheffler, *Phys. Rev. B* **46**, 16067 (1992).
- J. F. Janak and A. R. Williams, *Phys. Rev. B* **14**, 4199 (1976).
- C. S. Wang and J. Callaway, *Phys. Rev. B* **15**, 298 (1977).
- V. L. Moruzzi, A. R. Williams, and J. F. Janak, *Phys. Rev. B* **15**, 2854 (1977).
- K. Schwarz and P. Mohn, *J. Phys. F* **14**, L129 (1984).
- V. L. Moruzzi, P. M. Marcus, K. Schwarz, and P. Mohn, *Phys. Rev. B* **34**, 1784 (1986).
- C.-L. Fu and K.-M. Ho, *Phys. Rev. B* **28**, 5480 (1983).
- D. Singh, *Planewaves, Pseudopotentials and the LAPW Method* (Kluwer Academic, DO 1994), 115 pp.
- V. I. Anisimov, J. Zaanen, and O. K. Andersen, *Phys. Rev. B* **44**, 943 (1991).
- V. I. Anisimov, F. Aryasetiawan, and A. I. Liechtenstein, *J. Phys.: Condens. Matter* **9**, 767 (1997).
- J. P. Perdew and A. Zunger, *Phys. Rev. B* **23**, 5048 (1981).

45. DoD: Department of Defense-planewave; URL: <http://cst-www.nrl.navy.mil/people/singh/planewave>.
46. The ABINIT code is a common project of the Universite Catholique de Louvain, Corning Incorporated, and other contributors; URL: <http://www.mapr.ucl.ac.be/ABINIT>.
47. G. Theurich, B. Anson, N. A. Hill, and A. Hill, Computing in Science and Engineering, p. 22, Jan/Feb 2001. SPINOR is publicly available at <http://spinor.sourceforge.net>.
48. <http://www.gnu.org/copyleft/gpl.txt>.
49. VASP: Vienna Ab initio Simulation Package; URL: <http://cms.mpi.univie.ac.at/vasp/>.
50. <http://www.accelrys.com>.
51. M. C. Payne, X. Weng, B. Hammer, G. Francis, U. Bertram, A. de Vita, J. S. Lin, V. Milman, and A. Qteish, unpublished manuscript.
52. P. Ordejón, D. Sánchez-Portal, E. Artacho, and J. M. Soler, SIESTA: Spanish Initiative for Electronic Simulations with Thousands of Atoms; URL: <http://www.uam.es/siesta/>.
53. D. Sánchez-Portal, P. Ordejón, E. Artacho, and J. M. Soler, *Internat. J. Quantum Chem.* **65**, 453 (1997), and references therein.
54. O. K. Anderson, *Phys. Rev. B* **12**, 3060 (1975).
55. J. Korringa, *Physica* **13**, 392 (1947); W. Kohn and N. Rostocker, *Phys. Rev.* **94**, 1111 (1954).
56. P. Blaha, K. Schwarz, and J. Luitz, WIEN97: A Full Potential Linearized Augmented Plane Wave Package for Calculating Crystal Properties (Karlheinz Schwarz, Techn. Univ. Wien, Vienna, 1999). ISBN 3-9501031-0-4. See also URL: <http://www.tuwien.ac.at/theochem/wien97>.
57. <http://www.mpi-stuttgart.mpg.de/andersen/>.
58. M. Shirai, T. Ogawa, I. Kitagawa, and N. Suzuki, *J. Magn. Magn. Mater.* **177-181**, 1383 (1998).
59. T. Ogawa, M. Shirai, N. Suzuki, and I. Kitagawa, *J. Magn. Magn. Mater.* **196/197**, 428 (1999).
60. S. Sanvito and N. A. Hill, *Phys. Rev. B* **62**, 15553 (2000).
61. M. Shirai, *Physica E* **10**, 143 (2001).
62. A. Continenza, S. Picozzi, W. T. Geng, and A. J. Freeman, *Phys. Rev. B* **64**, 085204 (2001).
63. M. Jain, L. Kronik, J. R. Chelikowsky, and V. V. Godlevsky, *Phys. Rev. B* **64**, 245205 (2001).
64. J. H. Park, S. K. Kwon, and B. I. Min, *J. Magn. Magn. Mater.* **281/282**, 703 (2000).
65. B. I. Min, private communication (2001).
66. J. R. Schrieffer and P. A. Wolff, *Phys. Rev.* **149**, 491 (1966).
67. G. Theurich and N. A. Hill, *Phys. Rev. B* **64**, 073106 (2001).
68. S. Sanvito, P. Ordejón, and N. A. Hill, *Phys. Rev. B* **63**, 165206 (2001).
69. T. C. Schulthess and W. H. Butler, *J. Appl. Phys.* **89**, 7021 (2001).
70. M. van Schilfgaarde and O. N. Mryasov, *Phys. Rev. B* **63**, 233205 (2001).
71. Y.-J. Zhao, W. T. Geng, K. T. Park, and A. J. Freeman, *Phys. Rev. B* **64**, 035207 (2001).
72. H. Akai, *Phys. Rev. Lett.* **81**, 3002 (1998).
73. R. S. Mulliken, *J. Chem. Phys.* **23**, 1833 (1955).
74. R. S. Mulliken, *J. Chem. Phys.* **23**, 1841 (1955).
75. H. Ohldag, V. Solinus, F. U. Hillebrecht, J. B. Goedkoop, M. Finazzi, F. Matsukura, and H. Ohno, *Appl. Phys. Lett.* **76**, 2928 (2000).
76. J. K. Furdyna and J. Kossut, eds., *Semiconductor and Semimetals, Vol. 25: Diluted Magnetic Semiconductors* (Academic, New York, 1988); M. Balkanski and M. Averous, eds., *Diluted Magnetic Semiconductors* (Plenum, New York, 1991).
77. V. G. Abrammishvili, S. I. Gubarev, A. V. Komarov, and S. M. Ryabchenko, *Fiz. Tverd. Tela* **26**, 1095 (1984) [*Sov. Phys. Solid State* **26**, 666 (1984)].
78. S. I. Gubarev and M. G. Tyazhlov, *Fiz. Tverd. Tela* **32**, 635 (1990) [*Sov. Phys. Solid State* **32**, 373 (1990)].
79. S. I. Gubarev and M. G. Tyazhlov, *Pis'ma Zh. Eksp. Teor. Fiz.* **44**, 385 (1986) [*JEPT Lett.* **44**, 494 (1986)].
80. C. Benoit à la Guillaume, D. Scalbert, and T. Dietl, *Phys. Rev. B* **46**, 9853 (1992).
81. A. Oiwa, S. Kutumoto, A. Endo, M. Hirasawa, Y. Iye, H. Ohno, F. Matsukura, A. Shen, and Y. Sugawara, *Solid State Commun.* **103**, 209 (1997).
82. S. B. Zhang, S.-H. Wei, and A. Zunger, *Phys. Rev. B* **52**, 13975 (1995).
83. A. Chattopadhyay, S. Das Sarma, and A. J. Millis, cond-mat/0106455.
84. P. Specht, R. C. Lutz, R. Zhao, E. R. Weber, W. K. Liu, K. Bacher, F. J. Towner, T. R. Stewart, and M. Luysberg, *J. Vac. Sci. Technol. B* **17**, 1200 (1999).
85. S. Sanvito and N. A. Hill, *Appl. Phys. Lett.* **78**, 3493 (2001).
86. S. Sanvito and N. A. Hill, *J. Mag. Mag. Mater.* (submitted-a).
87. S. Sanvito and N. A. Hill, *J. Mag. Mag. Mater.* (submitted-b).
88. P. W. Anderson, *Phys. Rev.* **79**, 350 (1950).
89. H. Akai and P. H. Dederichs, *Phys. Rev. B* **47**, 8739 (1993).
90. P.-G. de Gennes, *Phys. Rev.* **118**, 141 (1960).
91. J. Dabrowski and M. Scheffler, *Phys. Rev. B* **40**, 10391 (1989).
92. M. Scheffler, F. Beeler, O. Jepsen, O. Gunnarsson, O. K. Andersen and G. B. Bachelet, in *Proceedings of the 13th International Conference on Defects in Semiconductors*, L. C. Kimerling and J. M. Parsey Jr., eds. (The Metallurgical Society of AIME, New York, 1984), p. 45.
93. G. Zanelatto, T. Kreutz, R. K. Kawakami, E. Johnston-Halperin, E. Gwinn, D. D. Awschalom, and A. C. Gossard, *Bull. Am. Phys. Soc.* **46**, 509 (2001).
94. T. Kreutz, G. Zanelatto, R. K. Kawakami, E. Johnston-Halperin, E. Gwinn, D. D. Awschalom, and A. C. Gossard, *Bull. Am. Phys. Soc.* **46**, 510 (2001).
95. S. Sanvito and N. A. Hill, cond-mat/0108406.
96. S. Sanvito, C. J. Lambert, J. H. Jefferson, and A. M. Bratkovsky, *Phys. Rev. B* **59**, 11936 (1999).
97. R. Moriya, Y. Katsumata, Y. Takatani, S. Haneda, T. Kondo, and H. Munekata, *Physica E* **10**, 224 (2001).
98. H. Saito, W. Zaets, R. Akimoto, K. Ando, Y. Mishima, and M. Tanaka, *J. Appl. Phys.* **89**, 7392 (2001).
99. H. Akinaga, T. Manago, and M. Shirai, *Jpn. J. Appl. Phys.* **39**, L1118 (2000).
100. K. Sato and H. Katayama-Yoshida, *Jpn. J. Appl. Phys.* **40**, L485 (2001).
101. L. Kronik, M. Jain, and J. R. Chelikowsky, preprint.
102. M. Zając, J. Gosk, M. Kamińska, A. Twardowski, T. Szyszko, and S. Podsiadlo, *Appl. Phys. Lett.* **79**, 2432 (2001).
103. K. Sato and H. Katayama-Yoshida, *Jpn. J. Appl. Phys.* **39**, L555 (2000).
104. K. Sato and H. Katayama-Yoshida, *Jpn. J. Appl. Phys.* **40**, L334 (2001).
105. K. Sato and H. Katayama-Yoshida, *Physica E* **10**, 251 (2001).
106. T. Wakano, N. Fujimura, Y. Morinaga, N. Abe, A. Ashida, and T. Ito, *Physica E* **10**, 260 (2001).
107. K. Sato and H. Katayama-Yoshida, *Jpn. J. Appl. Phys.* **40**, L651 (2001).
108. H. Shoren, F. Ikemoto, K. Yoshida, N. Tanaka, and K. Motizuki, *Physica E* **10**, 242 (2001).
109. Y. J. Zhao, W. T. Geng, A. J. Freeman, and T. Oguchi, *Phys. Rev. B* **63**, 201202 (2001).
110. Y. J. Zhao, S. Picozzi, A. Continenza, W. T. Geng, and A. J. Freeman, preprint.
111. P. Mahadevan and A. Zunger, cond-mat/0111570.
112. A. Svane and O. Gunnarsson, *Phys. Rev. Lett.* **65**, 1148 (1990).
113. D. Vogel, P. Krüger, and J. Pollmann, *Phys. Rev. B* **54**, 5495 (1996).